

1 **Development and evaluation of the interactive Model for Air Pollution and Land**  
2 **Ecosystems (iMAPLE) version 1.0**

3  
4 Xu Yue<sup>1#</sup>, Hao ~~Zhou~~<sup>1</sup>~~Zhou~~<sup>2,3#</sup>, Chenguang Tian<sup>1</sup>, Yimian ~~Ma~~<sup>2</sup>~~Ma~~<sup>4</sup>, Yihan Hu<sup>1</sup>, Cheng  
5 ~~Gong~~<sup>2</sup>~~Gong~~<sup>4</sup>, Hui ~~Zheng~~<sup>3</sup>~~Zheng~~<sup>5</sup>, Hong Liao<sup>1</sup>

6  
7 <sup>1</sup>Jiangsu Key Laboratory of Atmospheric Environment Monitoring and Pollution  
8 Control, Collaborative Innovation Center of Atmospheric Environment and Equipment  
9 Technology, School of Environmental Science and Engineering, Nanjing University of  
10 Information Science & Technology (NUIST), Nanjing, 210044, China

11 <sup>22</sup>[College of Meteorology and Oceanography, National University of Defense](#)  
12 [Technology, Changsha, 410073, China](#)

13 <sup>3</sup>[High Impact Weather Key Laboratory of China Meteorological Administration \(CMA\),](#)  
14 [Changsha, 410073, China](#)

15 <sup>4</sup>Department Biogeochemical Integration, Max Planck Institute for Biogeochemistry,  
16 Jena, 07745, Germany

17 <sup>35</sup>Key Laboratory of Regional Climate-Environment Research for Temperate East Asia,  
18 Institute of Atmospheric Physics, Chinese Academy of Sciences, Beijing, 100029,  
19 China

20  
21  
22 Corresponding authors: Xu Yue ([yuxu@nuist.edu.cn](mailto:yuxu@nuist.edu.cn))

23 ~~[Hong Liao \(\[hongliao@nuist.edu.cn\]\(mailto:hongliao@nuist.edu.cn\)\)](mailto:hongliao@nuist.edu.cn)~~

24  
25  
26 # These authors contribute equally

27

## Abstract

28  
29 Land ecosystems are important sources and sinks of atmospheric components. In turn,  
30 air pollutants affect the exchange rates of carbon and water fluxes between ecosystems  
31 and atmosphere. However, these biogeochemical processes are usually not well  
32 presented in the Earth system models, limiting the explorations of interactions between  
33 land ecosystems and air pollutants from the regional to global scales. Here, we develop  
34 and validate the interactive Model for Air Pollution and Land Ecosystems (iMAPLE)  
35 by upgrading the Yale Interactive terrestrial Biosphere model with process-based water  
36 cycles, fire emissions, wetland methane (CH<sub>4</sub>) emissions, and the trait-based ozone (O<sub>3</sub>)  
37 damages. Within the iMAPLE, soil moisture and temperature are dynamically  
38 calculated based on the water and energy balance in soil layers. Fire emissions are  
39 dependent on dryness, lightning, population, and fuel load. Wetland CH<sub>4</sub> is produced  
40 but consumed through oxidation, ebullition, diffusion, and plant-mediated transport.  
41 The trait-based scheme unifies O<sub>3</sub> sensitivity of different plant functional types (PFTs)  
42 with the leaf mass per area. Validations show correlation coefficients (*R*) of 0.59-0.86  
43 for gross primary productivity (GPP) and 0.57-0.84 for evapotranspiration (ET) across  
44 the six PFTs at 201 flux tower sites, and yield an average *R* of 0.68 for CH<sub>4</sub> emissions  
45 at 44 sites. Simulated soil moisture and temperature match reanalysis data with the high  
46 *R* above 0.86 and low normalized mean biases (NMB) within 7%, leading to reasonable  
47 simulations of global GPP (*R*=0.92, NMB=1.3%) and ET (*R*=0.93, NMB=-10.4%)  
48 against satellite-based observations for 2001-2013. The model predicts an annual global  
49 area burned of 507.1 Mha, close to the observations of 475.4 Mha with a spatial *R* of  
50 0.66 for 1997-2016. The wetland CH<sub>4</sub> emissions are estimated to be 153.45 Tg [CH<sub>4</sub>]  
51 yr<sup>-1</sup> during 2000-2014, close to the multi-model mean of 148 Tg [CH<sub>4</sub>] yr<sup>-1</sup>. The model  
52 also shows reasonable responses of GPP and ET to the changes in diffuse radiation, and  
53 yields a mean O<sub>3</sub> damage of 2.9% to global GPP. The iMAPLE provides an advanced  
54 tool for studying the interactions between land ecosystem and air pollutants.

55  
56 **Keywords:** carbon fluxes, water cycle, fire emissions, methane emissions, ozone  
57 damage, diffuse radiation.

58 **1. Introduction**

59 As an important component on the Earth, land ecosystems regulate global carbon and  
60 water cycles. Every year, the [terrestrial](#) ecosystem assimilates ~120 Pg (1 Pg = 10<sup>15</sup> g)  
61 carbon from atmosphere through vegetation photosynthesis (Beer et al., 2010).  
62 However, most of ~~these~~[this](#) carbon uptake returns to atmosphere due to plant and soil  
63 ~~respirations~~[respiration](#) (Sitch et al., 2015), as well as other perturbations such as  
64 biomass burning and biogenic emissions (~~Carslaw et al., 2010; van der Werf et al.,~~  
65 ~~2010~~[\(van der Werf et al., 2010;Carslaw et al., 2010\)](#), leading to a net carbon sink of  
66 only ~2 Pg C yr<sup>-1</sup> (~~Friedlingstein et al., 2022~~[during 1960-2021 \(Friedlingstein et al.](#)  
67 ~~2022)~~[2022\)](#). Meanwhile, land ecosystems affect atmospheric moisture and soil wetness  
68 through both physical (e.g., evaporation and runoff) and physiological (e.g., leaf  
69 transpiration and root hydrological uptake) processes. Observations show that  
70 transpiration accounts for 80%-90% of the terrestrial evapotranspiration (ET) (Jasechko  
71 et al., 2013) and makes significant contributions to land precipitation especially over  
72 the tropical forests (~~Spraeklen et al., 2012~~[\(Spracklen et al., 2012\)](#).

73  
74 Different approaches have been applied to depict the spatiotemporal variations of  
75 ecosystem processes. The eddy covariance technique provides direct measurements of  
76 land carbon and water fluxes (Jung et al., 2011). However, the limited number and  
77 uneven distribution of ground sites results in large uncertainties in the upscaling of site-  
78 level fluxes to the global scale (Jung et al., 2020b). Satellite retrieval provides a unique  
79 tool for the continuous representations of land fluxes in both space and time (Worden  
80 et al., 2021). However, most of the ecosystem variables (e.g., gross primary productivity,  
81 GPP) can only be derived using available signals from remote sensing through  
82 empirical relationships (Madani et al., 2017). As a comparison, process-based models  
83 build physical parameterizations based on field and/or laboratory experiments and  
84 validate against the available *in situ* and satellite-based observations (~~Niu et al., 2011;~~  
85 ~~Castillo et al., 2012~~[\(Niu et al., 2011;Castillo et al., 2012\)](#). These models can be further  
86 applied at different spatial (from site to global) and temporal (from days to centuries)

87 scales to identify the main drivers of the changes in carbon and water fluxes (Sitch et  
88 al., 2015). For example, a total of 17 vegetation models were validated and combined  
89 to predict the land carbon fluxes in the past century (~~Friedlingstein et al.,~~  
90 ~~2022~~)([Friedlingstein et al., 2022](#)); the ensemble mean of these models revealed a  
91 steadily increasing land carbon sink from 1960 with the dominant contribution by CO<sub>2</sub>  
92 fertilization.

93

94 While many studies quantified the ecosystem responses to the effects of CO<sub>2</sub>, climate,  
95 and human activities (~~Piao et al., 2009; Sitch et al., 2015~~)([Piao et al., 2009; Sitch et al.,](#)  
96 [2015](#)), few have explored the interactions between air pollution and land ecosystems.  
97 Such biogeochemical processes become increasingly important in the Anthropocene  
98 period with significant changes in atmospheric compositions. For example,  
99 observations found that nitrogen and phosphorus constrain the CO<sub>2</sub> fertilization  
100 efficiency of global vegetation (Terrer et al., 2019), but such limiting effect is ignored  
101 or underestimated in most of the current models (Wang et al., 2020). Tropospheric  
102 ozone (O<sub>3</sub>) damages plant photosynthesis and stomatal conductance, inhibiting carbon  
103 assimilation and the ET from the land surface (~~Sitch et al., 2007; Lombardozzi et al.,~~  
104 ~~2015~~)([Sitch et al., 2007; Lombardozzi et al., 2015](#)). Atmospheric aerosols can enhance  
105 photosynthesis through diffuse fertilization effects (Mercado et al., 2009) but  
106 meanwhile decrease photosynthesis by reducing precipitation (~~Yue et al., 2017~~)([Yue et](#)  
107 [al., 2017](#)). In turn, ecosystems act as both the sources and sinks of atmospheric  
108 components. Biomass burning emits a large amount of carbon dioxide, trace gases, and  
109 particulate ~~mattersmatter~~, further influencing air quality (~~Chen et al., 2021~~)([Chen et al.,](#)  
110 [2021](#)), ecosystem functions (~~Yue and Unger, 2018~~)([Yue and Unger, 2018](#)), and global  
111 climate (~~Fian et al., 2022~~)([Tian et al., 2022](#)). Biogenic volatile organic compounds  
112 (BVOCs) are important precursors for both surface O<sub>3</sub> and secondary organic aerosols  
113 (Wu et al., 2020), which can feed back to affect biogenic emissions (Yuan et al., 2016)  
114 and carbon ~~assimilationsassimilation~~ (Rap et al., 2018). Wetland methane (CH<sub>4</sub>)  
115 emissions account for the dominant fraction of natural sources of CH<sub>4</sub>, and are projected

116 to increase under the global warming scenarios (~~Zhang et al., 2017; Rosentreter et al.,~~  
117 ~~2021~~);(~~Rosentreter et al., 2021;Zhang et al., 2017~~). On the other hand, stomatal uptake  
118 dominates the dry deposition of air pollutants over the vegetated land (Lin et al., 2020).  
119 Meanwhile, ET from forest results in the increase of water vapor in atmosphere  
120 (~~Spracklen et al., 2012~~)(~~Spracklen et al., 2012~~), affecting the consequent rainfall and  
121 wet deposition of particles.

122

123 Currently, numerical models are in general developed separately for atmospheric  
124 chemistry and ecosystem processes. The chemical transport models are usually driven  
125 with prescribed emissions of biomass burning (Warneke et al., 2023) and wetland  
126 methane (Heimann et al., 2020), while the ecosystem models often ignore the  
127 biogeochemical impacts of O<sub>3</sub> and aerosols (~~Friedlingstein et al., 2022~~);(~~Friedlingstein~~  
128 ~~et al., 2022~~). In an earlier study, we developed and validated the Yale Interactive  
129 terrestrial Biosphere (YIBs) model version 1.0 with the special focus on the interactions  
130 between atmospheric chemistry and land ecosystems (~~Yue and Unger, 2015~~)(~~Yue and~~  
131 ~~Unger, 2015~~). Thereafter, the YIBs model has been used offline to assess the O<sub>3</sub>  
132 vegetation damage (~~Yue et al., 2016~~)(~~Yue et al., 2016~~), aerosol diffuse fertilization (~~Yue~~  
133 ~~and Unger, 2017~~)(~~Yue and Unger, 2017~~), ~~BVOCs emissions (Cao et al., 2021a)~~~~BVOC~~  
134 ~~emissions (Cao et al., 2021a)~~, as well as coupled to other models to investigate the  
135 carbon-chemistry-climate interactions (~~Lei et al., 2020; Gong et al., 2021~~);(~~Lei et al.,~~  
136 ~~2020;Gong et al., 2021~~). The YIBs model has joined the multi-model intercomparison  
137 project of TRENDY since the year 2020 and showed reasonable performance in the  
138 simulation of carbon fluxes (~~Friedlingstein et al., 2020~~)(~~Friedlingstein et al., 2020~~).  
139 However, the YIBs model failed to predict the typical hydrological variables such as  
140 ET and runoff due to the missing of carbon-water coupling modules. Furthermore, the  
141 model did not consider the nutrient limitation on plant photosynthesis and ignored some  
142 key exchange fluxes between land and atmosphere.

143

144 In this study, we develop the interactive Model for Air Pollution and Land Ecosystems

Formatted: Font: Not Bold

Formatted: Font: Not Bold

Formatted: Font: Not Bold

Formatted: Font: Not Bold

Formatted: Font: Not Bold

Formatted: Font: Not Bold

145 (iMAPLE) by coupling the process-based water cycle module from Noah-MP (Niu et  
146 al., 2011) to the carbon cycle in the YIBs (Figure 1). In addition, we update the original  
147 YIBs model with some major advances in the biogeochemical processes including  
148 dynamic fire emissions, wetland CH<sub>4</sub> emissions, nutrient limitations on photosynthesis,  
149 and the trait-based O<sub>3</sub> vegetation damage. The detailed descriptions of these updates  
150 are presented in the next section. The iMAPLE is fully validated against available  
151 measurements in Section 3. The last section will summarize the model performance and  
152 rethink the prospective directions for future development.

153

## 154 **2. Models and data**

### 155 **2.1 Main features of YIBs model**

156 The YIBs model is a process-based vegetation model predicting land carbon fluxes with  
157 dynamic changes in tree height, leaf area index, and carbon pools (~~Yue and Unger, 2015,~~  
158 ~~thereafter YU2015~~)(Yue and Unger, 2015, thereafter YU2015). A total of nine plant  
159 functional types (PFTs) are considered including evergreen broadleaf forest (EBF),  
160 evergreen needleleaf forest (ENF), deciduous broadleaf forest (DBF), tundra, shrubland,  
161 C<sub>3</sub>/C<sub>4</sub> grassland, and C<sub>3</sub>/C<sub>4</sub> cropland. At each grid, a mixture of PFTs with each PFT  
162 fraction is used as model input, sharing the temperature or moisture information from  
163 the same soil column. Leaf photosynthesis is calculated using the well-established  
164 Michaelis-Menten enzyme-kinetics scheme (~~Farquhar et al., 1980~~)(Farquhar et al.,  
165 1980) and is coupled to stomatal conductance with the modulations of air humidity and  
166 CO<sub>2</sub> concentrations (Ball et al., 1987). The model applies a two-leaf approach to  
167 distinguish the irradiating states for sunlit and shading leaves and adopts an adaptive  
168 stratification for the radiative transfer processes within canopy layers (Spitters, 1986).  
169 The gross carbon assimilation is further regulated by the optimized plant phenology,  
170 which is mainly dependent on temperature and light for deciduous trees (~~Yue et al.,~~  
171 ~~2015~~)(Yue et al., 2015) but temperature and/or moisture for shrubland and grassland  
172 (YU2015). The assimilated carbon is allocated among leaf, stem, and root to support  
173 autotrophic respiration and development, the latter of which is used to update plant

174 height and leaf area (Cox, 2001). The input of litterfall triggers the carbon transition  
175 among 12 soil carbon pools and determines the magnitude of heterotrophic respiration  
176 with the joint effects of soil temperature, moisture, and texture (Schaefer et al., 2008).  
177 The net carbon uptake is then calculated by subtracting ecosystem respiration (plant  
178 and soil) and environmental perturbations (reforestation or deforestation) from the  
179 gross carbon assimilation (~~Yue et al., 2021~~)([Yue et al., 2021](#)). The YIBs model  
180 reasonably reproduces the observed spatiotemporal patterns of global carbon fluxes and  
181 makes contributions to the Global Carbon Project with the long-term simulations of  
182 land carbon sink in the past century (~~Friedlingstein et al., 2020~~)([Friedlingstein et al.](#)  
183 [2020](#)). The model specifically considers air pollution impacts on land ecosystems  
184 (Figure 1), such as the ozone vegetation damage (~~Yue and Unger, 2014~~)([Yue and Unger,](#)  
185 [2014](#)) and aerosol diffuse fertilization effect (~~Yue and Unger, 2017~~)([Yue and Unger,](#)  
186 [2017](#)). The YIBs implements two different schemes for BVOCs emissions (Figure 1),  
187 including the Model of Emissions of Gases and Aerosols from Nature (MEGAN,  
188 Guenther et al., 2012) and the photosynthesis-dependent (PS\_BVOC) scheme (Unger  
189 et al., 2013).

190

## 191 **2.2 New processes in iMAPLE model**

### 192 2.2.1 Process-based water cycles

193 [The descriptions and units of all parameters used in this study are shown in Table S1.](#)

194 We implement the hydrological module from Noah-MP into the iMAPLE model (Niu  
195 et al., 2011). The water budget closure is achieved by constructing water-balance  
196 equations among precipitation ( $P$ ,  $\text{Kg m}^{-2} \text{s}^{-1}$ ), evapotranspiration ( $ET$ ,  $\text{Kg m}^{-2} \text{s}^{-1}$ ),  
197 runoff, and terrestrial water storage change ( $\Delta TWS$ ) on each grid cell as follows:

$$198 \quad P = ET + runoff + \Delta TWS \quad (1)$$

199 Here, hourly  $P$  from MERRA-2 reanalyses is used as the input.

200

201 We then divide  $ET$  into three portions including plant transpiration ( $TRA$ ), canopy  
202 evaporation ( $ECAN$ ) and ground evaporation ( $EGRO$ ):

203 
$$ET = TRA + ECAN + EGRO \quad (2)$$

204 For vegetated grids,  $TRA$  is calculated as follows:

205 
$$TRA = \frac{\rho_{air} \cdot CP_{air} \cdot C_{tra} \cdot (e_{sat} - e_{ca})}{PC} \quad (3)$$

206 where  $\rho_{air}$  is air density,  $CP_{air}$  is heat capacity of dry air, and  $PC$  is the psychrometric  
 207 constant.  $e_{sat}$  is the saturated vapor pressure at the leaf temperature,  $e_{ca}$  is the vapor  
 208 pressure of the canopy air and  $C_{tra}$  is leaf transpiration conductance, which is  
 209 calculated based on the Ball-Berry scheme of stomatal resistance (Yue and Unger,  
 210 2015)(Yue and Unger, 2015). Meanwhile,  $ECAN$  is calculated as follows:

211 
$$ECAN = \frac{\rho_{air} \cdot CP_{air} \cdot C_{canopy, evap} \cdot (e_{sat} - e_{ca})}{PC} \quad (4)$$

212 
$$C_{canopy, evap} = \frac{f_{wet} \cdot E_{VAI}}{R_{leaf, bdy}} \quad (5)$$

213 Here,  $C_{canopy, evap}$  is the latent heat conductance from the wet leaf surface to canopy  
 214 air.  $f_{wet}$  is the wetted fraction of canopy, which is a fraction of the maximum canopy  
 215 precipitation interception capacity.  $E_{VAI}$  is the effective vegetation area index and  
 216  $R_{leaf, bdy}$  is bulk leaf boundary resistance.  $EGRO$  is calculated as follows:

217 
$$EGRO = C_{ground, evap} (e_{sat, ground} RH - e_{ca}) \quad (6)$$

218 Here,  $C_{ground, evap}$  is the coefficient for latent heat at the ground,  $e_{sat, ground}$  is the  
 219 saturated vapor pressure at the ground and  $RH$  is the surface relative humidity.

220

221 Runoff includes surface ( $R_{srf}$ ) and subsurface ( $R_{sub}$ ) components:

222 
$$runoff = R_{srf} + R_{sub} \quad (47)$$

223 The surface runoff is calculated as follows:

224 
$$R_{srf} = Q_{soil, srf} - Q_{soil, in} \quad (58)$$

225 where  $Q_{soil, srf}$  is the incident water in the soil surface and is the sum of the  
 226 precipitation, snowmelt and dewfall.  $Q_{soil, in}$  is the infiltration into the soil, which is  
 227 derived from approximate solutions of Richards equations with considerations of the  
 228 spatial variations in precipitation and infiltration capacity. Here, we assume  
 229 independent and exponential distributions of infiltration capacity and precipitation in  
 230 each grid cell when considering soil infiltration processes and  $Q_{soil, in}$  is the infiltration



231 ~~into the soil,~~ following the approach by Schaake et al. (1996):

$$232 \quad Q_{soil,in} = Q_{soil,srf} \frac{I_c}{Q_{soil,srf} \Delta t + I_c} \quad (9)$$

$$233 \quad I_c = W_d [1 - \exp(-K_{\Delta t} \Delta t)] \quad (10)$$

234 Here,  $I_c$  and  $W_d$  are the soil infiltration capacity of the model grid cell and the water  
 235 deficit of the soil column, respectively.  $K_{\Delta t}$  and  $\Delta t$  are the calibratable parameters and  
 236 model time step. We assume free drainage processes in the soil column bottom, thus the

237  $R_{sub}$  is calculated as follows:

$$238 \quad R_{sub} = \alpha_{slope} \cdot K_4 \quad (11)$$

239 where  $\alpha_{slope} = 0.1$  is the terrain slope index.  $K_4$  is the hydraulic conductivity in the  
 240 bottom soil layer ~~from soil parameterizes used~~ parameterized following the scheme in  
 241 Clapp and Hornberger (1978).

242 and is calculated using spatial soil profiles from Hengl et al. (2017).

243

244 Terrestrial water storage ( $TWS$ ) is the sum of groundwater storage ( $W_{gw}$ ), soil water  
 245 content ( $W_{soil}$ ) and snow water equivalent ( $W_{snow}$ ):

$$246 \quad TWS = W_{gw} + W_{snow} + \sum_{i=1}^{N_{soil}} W_{soil} \quad (12)$$

247 Here, the soil module includes four layers ( $N_{soil} = 4$ ) and  ~~$W_{soil}$~~   $W_{soil}$  is calculated by the  
 248 volumetric water content ( $W_i$ ) as follows:

$$249 \quad \del{W_{soil}} W_{soil} = \rho_{wat} \cdot W_i \cdot \Delta Z_i \quad \text{for } i = 1, 2, 3, 4 \quad (13)$$

250 where water density ( $\rho_{wat}$ ) = 1000 kg m<sup>-3</sup>, and  $\Delta Z_i = 0.1, 0.3, 0.6$  and 1m, respectively.

251 Hourly  $W_i$  depends on variations of soil water diffusion ( $D$ ) and hydraulic conductivity  
 252 ( $K$ ) as follows:

$$253 \quad \frac{\partial W}{\partial t} = \frac{\partial}{\partial z} \left( D \frac{\partial W}{\partial z} \right) + \frac{\partial K}{\partial z} \quad (14)$$

254 Here,  $K$  and  $D$  are calculated following the parameterizations of Clapp-Hornberger  
 255 curves (Clapp and Hornberger, 1978):

$$256 \quad \frac{K}{K_{sat}} = \left( \frac{W}{W_{sat}} \right)^{2b+3} \quad (15)$$

$$257 \quad D = K \cdot \frac{\partial \phi}{\partial W} \quad (16)$$

258 
$$\frac{\varphi}{\varphi_{sat}} = \left(\frac{W}{W_{sat}}\right)^{-b} \quad (12) \quad (17)$$

259 where  $\varphi_{sat}$ ,  $W_{sat}$  and  $K_{sat}$  are saturated soil capillary potential, volumetric water  
 260 content and hydraulic conductivity. Exponent  $b$  is an empirical constant depending  
 261 on soil types. Soil moisture is calculated as the ratio of  $W_s$  to  $W_{sat}$ .

262

263 Soil temperature ( $T_s$ ) is calculated through physical processes as follows:

264 
$$\frac{\partial T_s}{\partial t} = \frac{1}{c} \frac{\partial}{\partial z} \left( K_T \frac{\partial T_s}{\partial z} \right) \quad (13) \quad (18)$$

265 Here  $K_T$  is soil specific heat capacity:

266 
$$K_T = K_e \cdot (K_s - K_{dry}) + K_{dry} \quad (14) \quad (19)$$

267 where  $K_e$ ,  $K_s$  and  $K_{dry}$  are Kersten values as a function of soil wetness, saturated soil  
 268 heat conductivity and that under dry air conditions (Niu et al., 2011).  $C$  in Equation (13)  
 269 is the specific heat

270 
$$C = W_{lip} \cdot C_{lip} + W_{ice} \cdot C_{ice} + (1 - W_{sat}) \cdot C_{sat} + (W_{sat} - W) \cdot C_{air} \quad (15) \quad (20)$$

271 Here,  $W_{lip}$ ,  $C_{lip}$  and  $W_{ice}$ ,  $C_{ice}$  indicate water content and heat capacity on soil water  
 272 and ice.  $C_{sat}$  and  $C_{air}$  are saturated and air heat capacity, which are empirical constants  
 273 (Niu et al., 2011).

274

### 275 2.2.2 Dynamic fire emissions

276 We implement the active global fire parameterizations from Pechony and Shindell  
 277 (2009) and Li et al. (2012) to the iMAPLE model. The fire emissions are determined  
 278 by several key factors such as fuel flammability, natural ignitions, human activities, and  
 279 fire spread. The fire count  $N_{fire}$  depends on flammability ( $Flam$ ), fire ignition (including  
 280 both natural ignition rate  $I_N$  and anthropogenic ignition rate  $I_A$ ) and anthropogenic  
 281 suppression ( $F_{NS}$ ):

282 
$$N_{fire} = Flam \times (I_N + I_A) \times F_{NS} \quad (16) \quad (21)$$

283  $Flam$  is a unitless metric representing conditions conducive to fire occurrence. It is  
 284 parameterized as a function of vapor pressure deficit (VPD), precipitation (Prec), and  
 285 leaf area index (LAI):

Formatted: Right

Formatted: Font color: Auto

Formatted: Font color: Auto

Formatted: Font color: Auto

Formatted: Font color: Auto

Formatted: Font color: Auto

Formatted: Font color: Auto

Formatted: Font color: Auto

Formatted: Font color: Auto

Formatted: Right

286 
$$Flam = VPD \times e^{-2 \times Prec} \times LAI \quad (17) \quad (22)$$

287  $I_N$  depends on the cloud-to-ground lightning and  $I_A$  can be expressed as:

288 
$$I_A = 0.03 \times PD \times k(PD) \quad (18) \quad (23)$$

289 where  $PD$  is population density. The empirical function of  $k(PD) = 6.8 \times PD^{-0.6}$  stands  
290 for ignition potentials by human activity. The fraction of non-suppressed fires  $F_{NS}$  is  
291 derived as:

292 
$$F_{NS} = 0.05 + 0.95 \times e^{-0.05 \times PD} \quad (19) \quad (24)$$

294 The burned area of a single fire ( $BA_{single}$ ) is typically taken to be elliptical in shape  
295 associated with near surface wind speed ( $U$ ) and relative humidity ( $RH$ ); length-to-  
296 breadth ratio ( $LB$ ), head-to-back ratio ( $HB$ ) and rate of fire spread ( $UP$ ) as follows;

297 
$$BA_{single} = \frac{\pi \times UP^2}{4 \times LB} \times \left(1 + \frac{1}{HB}\right)^2 \quad (20) \quad (25)$$

298 where Then,  $LB$  and  $HB$  are length-related to breadth ratio and head to back ratio,  
299 respectively; changes of near-surface wind speed ( $U$ ) as follows;

300 
$$LB = 1 + 10 \times (1 - e^{-0.06 \times U}) \quad (21) \quad (26)$$

301 
$$HB = \frac{LB + (LB^2 - 1)^{0.5}}{LB - (LB^2 - 1)^{0.5}} \quad (22) \quad (27)$$

302 The rate of fire spread (Meanwhile,  $UP$ ) is computed as: the function of relative  
303 humidity ( $RH$ ):

304 
$$UP = UP_{max} \times f_{RH} \times f_{\theta} \times G(W) \quad (23) \quad (28)$$

305 Here,  $UP_{max}$  is the maximum fire spread rate depending on PFTs,  $f_{RH}$  and  $f_{\theta}$  represent  
306 the dependence of fire spread on  $RH$  and on root-zone soil moisture, respectively.  $f_{\theta}$  is  
307 simply set to 0.5 and  $f_{RH}$  is calculated as:

308 
$$f_{RH} = \begin{cases} 0, & RH \leq RH_{low} \\ \frac{RH_{up} - RH}{RH_{up} - RH_{low}}, & RH_{low} < RH < RH_{up} \\ 1, & RH \geq RH_{up} \end{cases} \quad (24)$$

309 In this study, we set  $RH_{low} = 30\%$  and  $RH_{up} = 70\%$ .  $f_{RH} =$

310 
$$\begin{cases} 1, & RH \leq RH_{low} \\ \frac{RH - RH_{low}}{RH_{up} - RH_{low}}, & RH_{low} < RH < RH_{up} \\ 0, & RH \geq RH_{up} \end{cases} \quad (29)$$

311 In this study, we set  $RH_{low}=30\%$  and  $RH_{up}=70\%$  as the lower and upper thresholds of  
 312 RH following the methods used in Li et al. (2012). If RH is higher than 70%, natural  
 313 fires will not occur or spread, and RH will no longer be a constraint factor for fire  
 314 occurrence and spread if  $RH \leq 30\%$ .  $G(W)$  is the limit of the fire spread:

$$315 \quad G(W) = \frac{LB}{1 + \frac{1}{HB}} \quad (25) \quad (30)$$

316 In general, the eccentricity of burned area is primarily influenced by near-surface wind  
 317 speed, while the rate of fire spread is jointly regulated by near-surface wind speed and  
 318 relative humidity. The shape of the fire is converted to a circular form when the near-  
 319 surface wind speed reaches zero, and burning ceases to propagate once the relative  
 320 humidity is above a specific threshold.

321  
 322 Finally, the burned aera ( $BA$ ) is represented as:

$$323 \quad BA = BA_{single} \times N_{fire} \quad (26) \quad (31)$$

324 The fire-emitted trace gases and aerosols ( $Emis$ ) are calculated as:

$$325 \quad Emis = BA \times EF \quad (27) \quad (32)$$

326 where  $EF$  is the emission factors for different species (such as black carbon and organic  
 327 carbon aerosols). It is important to note that the feedbacks of fire activities on terrestrial  
 328 ecosystems have not been considered in the current version of iMAPLE model due to  
 329 the high complexity.

### 331 2.2.3 Wetland methane emissions

332 We implement the process-based wetland  $CH_4$  emissions into the iMAPLE model. The  
 333 anthropogenic sources of  $CH_4$  from Coupled Model Intercomparison Project phase 6  
 334 (CMIP6, <https://esgf-node.llnl.gov/projects/input4mips/>) are also used as input for  
 335 iMAPLE. For each soil layer, the flux of  $CH_4$  ( $F_{CH_4}$ ) is calculated as the difference  
 336 between production ( $P_{CH_4}$ ) and consumptions, which include oxidation ( $O_{CH_4}$ ),  
 337 ebullition ( $E_{CH_4}$ ), diffusion ( $D_{CH_4}$ ), and plant-mediated transport through aerenchyma  
 338 ( $A_{CH_4}$ ) as follows:

$$339 \quad F_{CH_4} = P_{CH_4} - O_{CH_4} - E_{CH_4} - D_{CH_4} - A_{CH_4} \quad (28) \quad (33)$$

Formatted: Font color: Auto  
 Formatted: Font color: Auto  
 Formatted: Font color: Auto  
 Formatted: Font color: Auto  
 Formatted: Right

Formatted: Font color: Auto  
 Formatted: Font color: Auto  
 Formatted: Font color: Auto  
 Formatted: Font color: Auto  
 Formatted: Font color: Auto  
 Formatted: Right  
 Formatted  
 Formatted: Font color: Auto  
 Formatted: Right

Formatted: Right

340 The net methane emission to the atmosphere is the sum of ebullition, diffusion and  
 341 aerenchyma transport from the top soil layer.

342

343 The production of CH<sub>4</sub> in soil depends on the quantity of carbon substrate and  
 344 environmental conditions including soil temperature  $T_s$ , pH, and wetland inundation  
 345 fraction  $f_{wetland}$  as follows:

$$346 \quad P_{CH_4} = R_h r f_{T_s} f_{pH} f_{wetland} \quad (29) \quad (34)$$

347 where  $R_h$  is the heterotrophic respiration estimated at the grid cell ( $mol\ C\ m^{-2}\ s^{-1}$ ).  $r$   
 348 represents the release ratio of methane and carbon dioxide (Wania et al., 2010). We  
 349 determine the dependence on  $T_s$  and soil pH in iMAPLE based on the parameterizations  
 350 from the TRIPLEX-GHG model (Zhu et al., 2014). The impact factor of soil  
 351 temperature  $f_{ST}$  can be calculated as follows (Zhang et al., 2002; Zhu et al., 2014):

$$352 \quad f_{ST} = \begin{cases} 0, & T_s < T_{min} \\ vt^{xt} \exp(xt(1-vt)), & T_{min} \leq T_s \leq T_{max} \\ 0, & T_s > T_{max} \end{cases} \quad (35)$$

$$353 \quad vt = (T_{max} - T_s) / (T_{max} - T_{opt}) \quad (36)$$

$$354 \quad xt = [\log(Q_{10}) (T_{max} - T_{opt})]^2 (1.0 + at^{0.5})^2 / 400.0 \quad (37)$$

$$355 \quad at = 1.0 + 40.0 / [\log(Q_{10}) (T_{max} - T_{opt})] \quad (38)$$

356  $T_{min}$ ,  $T_{max}$ , and  $T_{opt}$  represents the lowest, highest and optimum temperature for the  
 357 process of methane production and oxidation, respectively. In this study, the  $T_{min} =$   
 358  $0^\circ\text{C}$ ,  $T_{max} = 45^\circ\text{C}$  and  $T_{opt} = 25^\circ\text{C}$  (Zhu et al., 2014).

359

360 For the temperature-dependence, the  $Q_{10}$  relationships are applied as follows:

$$361 \quad Q_{10} = r_b Q_b^{\frac{T_s - T_{base}}{10}} \quad (30) \quad (39)$$

362 Here  $r_b$  is set to 3.0 and  $Q_b$  is 1.33 with a base temperature ( $T_{base}$ ) of  $25^\circ\text{C}$  (Zhu et al.,  
 363 2014; Paudel et al., 2016) (Zhu et al., 2014; Paudel et al., 2016). The inundation fraction  
 364 of wetland at each cell describes the proportion of anaerobic conditions (Zhang et al.,  
 365 2021). We ignore the impact of redox potential (Eh) because global observations are  
 366 not available and the Eh-related processes are poorly characterized in current models  
 367 (Wania et al., 2010).

Formatted: Right

Formatted: Right

368

369 The oxidation of CH<sub>4</sub> is a series of aerobic activities related to temperature and CH<sub>4</sub>  
370 concentrations:

371 
$$O_{CH_4} = [CH_4]f_{Ts}f_{CH_4} \quad (31) \quad (40)$$

372 where [CH<sub>4</sub>] is the methane amount in each soil layer ( $gCm^{-2}layer^{-1}$ ).  $f_{CH_4}$  is the  
373 CH<sub>4</sub> concentration factor representing a Michaelis-Menten kinetic relationship:

374 
$$f_{CH_4} = \frac{[CH_4]}{[CH_4] + K_{CH_4}} \quad (32) \quad (41)$$

375 where  $K_{CH_4} = 5 \mu mol L^{-1}$  is the half-saturation coefficient with respect to CH<sub>4</sub> (Walter  
376 and Heimann, 2000). For temperature-dependence of oxidation, the  $Q_{10}$  relationship  
377 with  $r_b = 2.0$ ,  $Q_b = 1.9$ , and  $T_{base} = 12^\circ C$  is adopted (Zhu et al., 2014; Paudel et al.,  
378 2016)(Zhu et al., 2014;Paudel et al., 2016).

379

380 The diffusion of CH<sub>4</sub> follows the Fick's law with dependence on CH<sub>4</sub> concentrations  
381 and the molecular diffusion coefficients of CH<sub>4</sub> in the air ( $D_a = 0.2 cm^2s^{-1}$ ) and water  
382 ( $D_w = 0.00002 cm^2s^{-1}$ ) respectively (Walter and Heimann, 2000). For each soil layer  
383  $i$ , the diffusion coefficient  $D_i$  can be calculated as follows :

384 
$$D_i = D_a \times (R_{sand} \times 0.45 + R_{silt} \times 0.2 + R_{clay} \times 0.14) \times f_{tort} \times S_{poro} \times (1 -$$
  
385 
$$WFPS_i) + D_w \times WFPS_i \quad (33) \quad (42)$$

386 where  $R_{sand}$ ,  $R_{silt}$ ,  $R_{clay}$  is the relative content of sand, silt, and clay in the soil,  $f_{tort} =$   
387 0.66 is tortuosity coefficient,  $S_{poro}$  is soil porosity, and  $WFPS$  represents the pore space  
388 full of water (Zhuang et al., 2004).

389

390 The ebullition of CH<sub>4</sub> occurs when CH<sub>4</sub> concentration is above the threshold of 0.5  
391  $mol CH_4m^{-3}$  (Walter et al., 2001). Since the process of ebullition occurs in a very short  
392 time, the bubbles will generate at once and all the flux will be released to atmosphere  
393 if the concentration reaches the threshold. The plant-mediated transport of CH<sub>4</sub> through  
394 aerenchyma is dependent on the concentration gradient of CH<sub>4</sub> and the plant-related  
395 factors (Zhu et al., 2014). The  $A_{CH_4}$  is determined by the oxidation factor of root and  
396 the aerenchyma factor of plant. The baseline value of the oxidation factor in root is 0.5.

with a regulatory range from 0.2 to 1.0 determined by the types of plant in wetland. The plant aerenchyma factor is calculated by the ratio of plant root length density (typical value: 2.1 cm mg<sup>-1</sup>) and root cross-sectional area (typical value: 0.0013 cm<sup>2</sup>), along with the diffusion factor of methane from plant root to atmosphere which is modulated by plant species within a range of 0 to 1 (Zhang et al., 2002).

#### 2.2.4 The down regulation on photosynthesis

We implement the down regulation parameterization from Arora et al. (2009) to indicate the nutrient limitations on leaf photosynthesis. A down-regulating factor  $\varepsilon$  is calculated as a function of CO<sub>2</sub> concentrations ( $C$ ) as follows:

$$\varepsilon(C) = \frac{1+\gamma_{gd}\ln(C/C_0)}{1+\gamma_g\ln(C/C_0)} \quad (34) \quad (43)$$

where  $C_0$  is a reference CO<sub>2</sub> concentration set to 288 ppm. The values of  $\gamma_{gd} = 0.42$  and  $\gamma_g = 0.90$  are derived from multiple measurements to constrain the CO<sub>2</sub> fertilization. Then the down-regulated photosynthesis is calculated by scaling the original value with the factor of  $\varepsilon$ .

#### 2.2.5 Trait-based O<sub>3</sub> vegetation damaging scheme

The YIBs model considers O<sub>3</sub> vegetation damage using the flux-based scheme proposed by ~~Sitch et al. (2007)~~ Sitch et al. (2007) (thereafter S2007), which determines the damaging ratio  $F$  of plant photosynthesis as follows:

$$F = a_{PFT} \times \max\{f_{O_3} - t_{PFT}, 0\} \quad (35) \quad (44)$$

Here, the  $f_{O_3}$  denotes O<sub>3</sub> stomatal flux (nmol m<sup>-2</sup> s<sup>-1</sup>) defined as:

$$f_{O_3} = \frac{[O_3]}{r + \left[ \frac{k_{O_3}}{g_p \times (1-F)} \right]} \quad (36) \quad (45)$$

where  $[O_3]$  represents the O<sub>3</sub> concentrations at the reference level (nmol m<sup>-3</sup>).  $r$  is the sum of boundary and aerodynamic resistance between leaf surface and reference level (s m<sup>-1</sup>).  $g_p$  is the potential stomatal conductance for H<sub>2</sub>O (m s<sup>-1</sup>).  $k_{O_3} = 1.67$  is a conversion factor of leaf resistance for O<sub>3</sub> to that for water vapor. The level of O<sub>3</sub> damage is then determined by the PFT-specific sensitivity  $a_{PFT}$  and threshold  $t_{PFT}$ , which are different among PFTs.

Formatted: Font color: Auto

Formatted: Right

Formatted: Right

Formatted: Right

426

427 In iMAPLE, we implement the trait-based O<sub>3</sub> vegetation damaging scheme to unify the  
428 inter-PFT sensitivities (Ma et al., 2023)(Ma et al., 2023):

429 
$$a_{PFT} = \frac{a}{LMA} \quad (37) \quad (46)$$

430 Here, a unified plant sensitivity  $a$  (nmol<sup>-1</sup> g s) is scaled by leaf mass per area (LMA, g  
431 m<sup>-2</sup>) to derive the sensitivity of a specific PFT ( $a_{PFT}$ ). Accordingly, the damaging  
432 fraction  $F$  is modified as follows:

433 
$$F = a \times \max \left\{ \frac{f_{O_3}}{LMA} - t, 0 \right\} \quad (38) \quad (47)$$

434 Here  $t$  (nmol g<sup>-1</sup> s<sup>-1</sup>) is a unified flux threshold for O<sub>3</sub> vegetation damage. The  $f_{O_3}$  in  
435 Equation (45) is fed into Equation (47) so as to build a quadratic equation for  $F$ . We  
436 solve the quadratic equation and select the  $F$  value within the range of [0, 1]. The  
437 updated scheme considers the dilution effects of O<sub>3</sub> dose through leaf cross-section by  
438 incorporating LMA. Plants with high LMA (e.g., ENF and EBF) usually have low  
439 sensitivities, and those with low LMA (e.g., DBF and crops) are more sensitive to O<sub>3</sub>  
440 damages. The unified sensitivity  $a$  is set to 3.5 nmol<sup>-1</sup> g s and threshold  $t$  is set to 0.019  
441 nmol g<sup>-1</sup> s<sup>-1</sup> by calibrating simulated  $F$  values with literature-based measurements (Ma  
442 et al., 2023)(Ma et al., 2023).

443

### 444 2.3 Design of simulations

445 We perform four sensitivity experiments with the iMAPLE model. The baseline (BASE)  
446 simulation considers the two-way coupling between carbon and water cycles, so that  
447 the prognostic soil meteorology drives canopy photosynthesis and evapotranspiration.  
448 A sensitivity run named BASE\_NW is set up by turning off the water cycle in the  
449 iMAPLE model. In this simulation, the soil moisture and soil temperature are adopted  
450 from the Modern-Era Retrospective Analysis for Research and Applications, Version 2  
451 (MERRA-2) reanalyses (Gelaro et al., 2017). The third and fourth runs turn on the O<sub>3</sub>  
452 vegetation damage effect using either the LMA-based scheme (O3LMA) or the S2007  
453 scheme (O3S2007). Surface hourly O<sub>3</sub> concentrations are adopted from the simulations  
454 with a chemical transport model used in our previous study (Yue and Unger, 2018). For

Formatted: Right

Formatted: Right



455 all simulations, the iMAPLE model is driven with the hourly surface meteorology at a  
456 spatial resolution of  $1^{\circ} \times 1^{\circ}$  from the MERRA-2 reanalyses, including surface air  
457 temperature, air pressure, specific humidity, wind speed, precipitation, snowfall,  
458 shortwave and longwave radiation. We run the model for the period of 1980-2021 using  
459 the initial conditions of the equilibrium soil carbon pool, tree height, and water fluxes  
460 from a spin-up run of 200 years. ~~driven with cycled forcing at the year 1980.~~

461

462 The iMAPLE model is driven with observed CO<sub>2</sub> concentrations from Mauna Loa  
463 (Keeling et al., 1976) and the land cover fraction of nine PFTs derived by combining  
464 satellite retrievals from both Moderate Resolution Imaging Spectroradiometer (MODIS)  
465 (Hansen et al., 2003) and Advanced Very High Resolution Radiometer (AVHRR)  
466 (~~Defries et al., 2000~~)([Defries et al., 2000](#)). For fire emissions, we use Gridded  
467 Population of the World version 4  
468 (<https://sedac.ciesin.columbia.edu/data/collection/gpw-v4>) to calculate human ignition  
469 and suppression. The ~~lightning~~ lightning ignition is calculated using the flash rate from  
470 Very High Resolution Gridded Lightning Climatology Data ~~Collection Version 1~~  
471 [CollectionVersion1](#) ([https://ghrc.nsstc.nasa.gov/uso/ds\\_details/collections/lisvhrcC.ht](https://ghrc.nsstc.nasa.gov/uso/ds_details/collections/lisvhrcC.html)  
472 ml). For wetland CH<sub>4</sub> emissions, we use the 2000-2020 global dataset of Wetland Area  
473 and Dynamics for Methane Modeling (WAD2M) derived from static datasets and  
474 remote sensing (Zhang et al., 2021), global soil pH from Hengl et al. (2017), and  
475 gridded soil texture from Scholes et al. (2011). For the LMA-based O<sub>3</sub> damage scheme,  
476 we use gridded LMA ~~derived~~ from the trait-level dataset of TRY (Kattge et al., 2011)  
477 ~~using developed by extending field measurements with~~ the random forest model  
478 (Moreno-Martínez et al., 2018).

479

#### 480 **2.4 Data for validations**

481 We use observational datasets to validate the biogeochemical processes and related  
482 variables simulated by the iMAPLE model. For simulated carbon and water fluxes, site-  
483 level observations are collected from ~~the 201 sites at the FLUXNET network~~ (Table

Formatted: Font color: Auto

484 ~~S1)-201 sites at the FLUXNET network (Table S2 and Figure 2). Among these sites, 95~~  
485 ~~are tree species with the major PFT of ENF and 106 are non-tree species with the~~  
486 ~~maximum number for shrubland. Most (71%) of sites are located at the middle latitudes~~  
487 ~~(30°-60°N) of the Northern Hemisphere (NH), especially in the U.S. and Europe.~~  
488 ~~Compared to the earlier evaluations in YU2015, we have many more sites in the tropics~~  
489 ~~(22 in this study vs. 5 in YU2015), Asia (20 in this study vs. 1 in YU2015), and Southern~~  
490 ~~Hemisphere (28 in this study vs. 7 in YU2015) in this study. We also use the global~~  
491 ~~gridded observations of GPP from the satellite retrievals including the solar-induced~~  
492 ~~chlorophyll fluorescence (SIF) product GOSIF (Li and Xiao, 2019) and the Global land~~  
493 ~~surface satellite (GLASS) product (Yuan et al., 2010). The global observations of ET~~  
494 ~~are adopted from the benchmark product of FLUXCOM (Jung et al., 2020a) and the~~  
495 ~~satellite-based GLASS product. For the dynamic fire module, we use monthly observed~~  
496 ~~area burned from the Global Fire Emission Database version 4.1 with small fires~~  
497 ~~(GFED4.1s) during 1997-2016 (van der Werf et al., 2010; Randerson et al., 2012)(van~~  
498 ~~der Werf et al., 2010; Randerson et al., 2012). For methane emissions, we use site-level~~  
499 ~~measurements of CH<sub>4</sub> fluxes from the FLUXNET-CH<sub>4</sub> network (Delwiche et al., 2021).~~  
500 ~~We exclude the monthly records with missing data at more than half of the days and~~  
501 ~~calculate the long-term mean fluxes for the seasonal cycle. In total, we select 44 sites~~  
502 ~~with at least six months of data available for the validations (Table S2). We also use the~~  
503 ~~anthropogenic sources of CH<sub>4</sub> from the archive of Coupled Model Intercomparison~~  
504 ~~Project phase 6 (CMIP6, <https://esgf.node.llnl.gov/projects/input4mips/>):S3).~~

505

### 506 **3. Model evaluations**

#### 507 3.1 Site-level evaluations

508 ~~We compare the simulated carbon and water fluxes to *in situ* measurements at 201~~  
509 ~~FLUXNET sites (Figure 2). Among these sites, 95 are tree species with the major PFT~~  
510 ~~of ENF and 106 are non-tree species with the maximum number for shrubland. Most~~  
511 ~~(71%) of sites are located at the middle latitudes (30°-60°N) of the Northern Hemisphere~~  
512 ~~(NH), especially in the U.S. and Europe. Compared to the earlier evaluations in~~

513 ~~YU2015, we have much more sites in the tropics (22 in this study vs. 5 in YU2015),~~  
514 ~~Asia (20 in this study vs. 1 in YU2015), and Southern Hemisphere (28 in this study vs.~~  
515 ~~7 in YU2015) in this study.~~

516

517 Simulated GPP shows correlation coefficients (R) of 0.59-0.86 for the six main PFTs  
518 with varied sample numbers (Figure 3). The highest R is achieved for ENF, though the  
519 model underestimates the mean GPP magnitude by 20.62% for this species. On average,  
520 simulated GPP is lower than observations for most PFTs. Compared to previous  
521 evaluations from the YIBs model, (YU2015), iMAPLE with coupled water cycle  
522 improves the R of GPP simulations for ENF (from 0.65 to 0.86) and grassland (from  
523 0.7 to 0.8) but worsens the predictions for other species, such as EBF (from 0.65 to  
524 0.59). The main cause of such deficit is the application of MERRA-2 reanalyses in the  
525 iMAPLE simulations instead of the site-level meteorology used in the YU2015. The  
526 biases in the meteorological input may cause uncertainties in the simulation of GPP  
527 fluxes (Ma et al., 2021). ~~Furthermore, the increase of site number and record length~~  
528 ~~may decrease the R to some extent.~~(Ma et al., 2021). ~~In addition, the mismatch of~~  
529 ~~vegetation cover and soil properties between the site location and 1°×1° grid in the~~  
530 ~~simulation may further contribute to the modeling biases.~~

531

532 Simulated ET matches observations with correlation coefficients of 0.57-0.84 at the  
533 FLUXNET sites (Figure 4). Relatively better performance is achieved for ENF (R=0.83)  
534 and grassland (R=0.84), for which the model yields good predictions of GPP as well.  
535 In contrast, low correlations and high biases are predicted for shrubland and cropland.  
536 For the shrubland sites, different land types (e.g., closed shrublands, permanent  
537 wetlands, and woody savannas) share the same parameters in the iMAPLE model,  
538 resulting in the biases in depicting the site-specific carbon and water fluxes. For  
539 cropland, the prognostic phenology of grass species is applied in the model due to the  
540 missing of plantation information for individual sites. Even with these deficits, the  
541 iMAPLE model in general captures the spatiotemporal variations of GPP and ET at

542 most sites.

543

544 We further compare the simulated wetland CH<sub>4</sub> fluxes from BASE experiment with  
545 observations at the FLUXNET-CH<sub>4</sub> sites. Similar to the carbon flux sites, most of these  
546 CH<sub>4</sub> flux sites are located in the NH (Figure 5a). However, different from the carbon  
547 fluxes which usually range from 0 to 15 g C m<sup>-2</sup> day<sup>-1</sup>, the CH<sub>4</sub> fluxes show a wide  
548 range across several orders of magnitude from 10<sup>-2</sup> to 10<sup>3</sup> g [CH<sub>4</sub>] m<sup>-2</sup> yr<sup>-1</sup> (Figure 5b).  
549 Such a large contrast requires a more realistic configuration of model parameters to  
550 distinguish the large gradient among sites. For example, US-Tw1 and US-~~Tw~~Tw4 are  
551 two nearby sites within a distance of 1 km, where our simulations present CH<sub>4</sub> flux of  
552 14.35 g[CH<sub>4</sub>] m<sup>-2</sup> yr<sup>-1</sup> during 2011-2017. However, average CH<sub>4</sub> flux shows a difference  
553 of 3.7 times with 66.31 g[CH<sub>4</sub>] m<sup>-2</sup> yr<sup>-1</sup> in US-Tw1 and 18.16 g[CH<sub>4</sub>] m<sup>-2</sup> yr<sup>-1</sup> in US-  
554 Tw4 during 2011-2017. In the model, these two sites share the same land surface  
555 properties because they are located on the same grid. On average, simulated CH<sub>4</sub> fluxes  
556 are correlated with observations at a moderate R of 0.68 and a normalized mean bias  
557 (NMB) of -28%.

558

### 559 3.2 Grid-level evaluations

560 The coupling of Noah-MP module enables the dynamic prediction of soil parameters  
561 by the iMAPLE model. We compare the simulated soil moisture and soil temperature  
562 from BASE experiment with MERRA-2 reanalyses (Figure 6). Both simulations  
563 (Figure 6a) and observations (Figure 6b) show low soil moisture over arid and semi-  
564 arid regions with the minimum in North Africa. The model also captures the high soil  
565 moisture in tropical rainforest. However, the prediction underestimates soil moisture in  
566 boreal regions in NH (Figure 6c). On the global scale, simulated soil moisture matches  
567 observations with a high R of 0.86 and a low NMB of -6.9%. These statistical metrics  
568 are further improved for the simulated soil temperature with the R of 0.99 and NMB of  
569 0.5% against observations (Figure 6f). The simulation reproduces the observed spatial  
570 pattern with a uniform warming bias.

571

572 Driven with the prognostic soil moisture and temperature, the iMAPLE model predicts  
573 reasonable land carbon and water fluxes (Figure 7). Simulated GPP (Figure 7a)  
574 reproduces observed patterns (Figure 7b) with high values in the tropical rainforest,  
575 moderate values in the boreal forests, and low values in the arid regions. On the global  
576 scale, our simulations yield a total GPP of 129.8 Pg C yr<sup>-1</sup>, similar to the observed  
577 amount of 125.4 Pg C yr<sup>-1</sup>. The predicted GPP is higher than observations over the  
578 tropical rainforest (Figure 7c). However, such overestimation may instead be an  
579 indicator of biases in the ensemble observations, which are derived from the empirical  
580 models instead of direct measurements (Running et al., 2004; Yuan et al., 2010);(Yuan  
581 et al., 2010;Running et al., 2004). Our site-level evaluations show that iMAPLE  
582 predicts reasonable GPP values at the EBF sites (Figure 3). Despite this inconsistency,  
583 the model yields a high R of 0.92 and a small NMB of 1.3% for GPP against  
584 observations on the global scale (Figure 7c). Simulated ET (Figure 7d) matches the  
585 observations (Figure 7e) with high values in the tropical rainforest and secondary high  
586 values in the boreal forest. In general, the prediction is lower than observations except  
587 for the eastern U.S. and eastern China (Figure 7f). On average, the iMAPLE model  
588 shows the R of 0.93 and NMB of -10.4% in the simulation of ET compared to the  
589 ensemble of observations.

590

591 We further compare the simulated GPP with (BASE) or without (BASE\_NW) dynamic  
592 water cycle (Figure 8). Relative to the simulations driven with MERRA-2 soil moisture  
593 and temperature, the iMAPLE model coupled with Noah-MP water module predicts  
594 very similar GPP over the hotspot regions such as tropical rainforest and boreal forest  
595 (Figure 8a). However, the coupled model predicts lower GPP for grassland in the tropics  
596 (e.g., South America and central Africa) but higher GPP in arid regions (e.g., South  
597 Africa and Australia). Since the baseline GPP is very low in arid regions, the relative  
598 changes are even larger than 100% over those areas. These GPP differences are mainly  
599 driven by the changes in soil moisture, which increases over the arid regions with the

600 dynamic water cycle (Figure 6c). The reduction of soil moisture in the high latitudes of  
601 NH shows limited impacts on the predicted GPP, likely because the boreal ecosystem  
602 is more dependent on temperature than moisture (Beer et al., 2010).

603

### 604 3.3 Ecosystem perturbations to air pollution

605 Within the iMAPLE framework, the land ecosystem perturbs atmospheric components  
606 through the emissions from biomass burning, wetland CH<sub>4</sub>, and BVOCs. We compare  
607 the simulated burned fraction and fire-emitted organic carbon (OC) emissions with  
608 observations from GFED4.1s (Figure 9). The largest burned fraction is predicted over  
609 the Sahel region and countries of Angola and Zambia, surrounding the low center of  
610 Congo rainforest. Moderate burnings could be found in northern Australia and eastern  
611 South America. Most of these hotspots are located on the grassland and shrubland in  
612 the tropics, where the high temperature and limited rainfall promotes regional fire  
613 activities. The model reasonably captures the observed fire pattern with a spatial  
614 correlation of 0.66 and NMB of 6.05% (Figure 9c), though the model overestimates the  
615 area burned in South Africa. The predicted fire area is used to derive biomass burning  
616 emissions of air pollutants (e.g., carbon monoxide, nitrogen oxides, black carbon,  
617 organic carbon, sulfur dioxide) with the specific emission factors (~~Tian et al.,~~  
618 2023)(Tian et al., 2023). Furthermore, we compare fire-emitted OC from the model  
619 with GFED4.1s. The spatial pattern of OC emissions is similar to that of burned area.  
620 The simulations yield a total of 16.8 Tg yr<sup>-1</sup> for the global fire-emitted OC, slightly  
621 higher than the amount of 16.4 Tg yr<sup>-1</sup> from GFED4.1s with some overestimations in  
622 tropical Africa (Figure 9f).

623

624 The wetland emissions of CH<sub>4</sub> show hotspots over tropical rainforests (Figure 10a),  
625 where the dense soil carbon provides abundant substrates for emissions and the warm  
626 climate promotes the emission rates. The secondary hotspots are located at the boreal  
627 regions in the NH. This spatial pattern is very similar to the map of wetland CH<sub>4</sub>  
628 emissions predicted by an ensemble of 13 biogeochemical models (Saunois et al., 2020).

629 On the global scale, the total wetland emission is 153.45 Tg [CH<sub>4</sub>] yr<sup>-1</sup> during 2000-  
630 2014, close to the average of 148±25 Tg [CH<sub>4</sub>] yr<sup>-1</sup> for 2000-2017 estimated by the  
631 multiple models. As a comparison, anthropogenic source of CH<sub>4</sub> show the high amount  
632 in China and India due to the large emissions from fossil fuels and agriculture (Figure  
633 10b). On the global scale, the wetland emissions are equivalent to 45.3% of the total  
634 anthropogenic emissions. [As important factors driving CH<sub>4</sub> emissions, heterotrophic](#)  
635 [respiration shows higher values over tropical regions and eastern China with a total](#)  
636 [amount of 73.2 Pg C yr<sup>-1</sup> \(Figure 10c\), and relative high wetland coverages are found](#)  
637 [in boreal Asia and Amazon \(Figure 10d\).](#)

638  
639 Isoprene emissions from the two schemes in the iMAPLE model show similar spatial  
640 distributions with the hotspots over tropical rainforest (Figure 11), where the warm  
641 climate and abundant light are favorable for the biogenic emissions. Compared to the  
642 MEGAN scheme, the PS\_BVOC scheme yields higher emissions in the tropical  
643 rainforest and boreal forest, but lower emissions for the shrubland and grassland in  
644 semiarid regions (Figure 11c). Such differences are attributed to the varied processes as  
645 well ~~weas~~ the emission factors. Our earlier study showed that PS\_BVOC scheme  
646 predicts stronger trends in isoprene emissions than MEGAN (~~Cao et al., 2021a~~)(Cao et  
647 [al., 2021a](#)), because the former considers both CO<sub>2</sub> fertilization and inhibition effects  
648 while the latter considers only the inhibition effects. On the global scale, isoprene  
649 emissions are 550 Tg yr<sup>-1</sup> with PS\_BVOC (Figure 11a) and 611 Tg yr<sup>-1</sup> with MEGAN  
650 (Figure 11b). These amounts are higher than the ensemble mean of 448 Tg yr<sup>-1</sup> from  
651 the CMIP6 models (~~Cao et al., 2021b~~)(Cao et al., 2021b), but in general within the  
652 range of 412-601 Tg yr<sup>-1</sup> as summarized by Carslaw et al. (2010).

653

#### 654 3.4. Air pollution impacts on ecosystem fluxes

655 We assess the damaging effects of surface O<sub>3</sub> to GPP with two schemes ([O3LMA –](#)  
656 [BASE and O3S2007 - BASE](#))(Figure 12). Simulated GPP losses show similar patterns  
657 with high damages in eastern U.S., western Europe, and eastern China, where surface

658 O<sub>3</sub> level is high due to the anthropogenic emissions. Limited GPP damages are  
659 predicted in the tropics though with abundant forest coverage due to the low level of  
660 O<sub>3</sub> pollution. Compared to the S2007 scheme, predicted GPP loss is further alleviated  
661 in tropical rainforest with the LMA-based scheme, because the latter scheme  
662 determines lower O<sub>3</sub> sensitivity for evergreen trees due to their higher content of  
663 chemical resistance with the larger LMA value (Ma et al., 2023)(Ma et al., 2023). On  
664 the global scale, the average GPP loss is -2.9% with the LMA scheme and -3.2% with  
665 the S2007 scheme. Such damage to GPP is weaker than the estimate of -4.8% in Ma et  
666 al. (2023)Ma et al. (2023) because of the differences in O<sub>3</sub> concentrations, vegetation  
667 types, and photosynthetic parameters.

668

669 Atmospheric aerosols cause perturbations to both direct and diffuse radiation, which  
670 have different efficiencies in enhancing plant photosynthesis. Here, we separate the  
671 diffuse (diffuse fraction > 0.75) and direct (diffuse fraction < 0.25) components of using  
672 observed diffuse fraction and solar radiation at six FLUXNET sites, and aggregate the  
673 GPP and ET fluxes for different radiation periods at certain intervals (Figure 13). At the  
674 six selected sites, observed GPP is higher and grows faster with more diffusive light  
675 than that under the direct light conditions (Figure 13a-13f). Simulations in general  
676 reproduce such feature with the comparable variability. In the earlier study, simulated  
677 diffuse fertilization efficiency for GPP (changes of GPP per unit diffuse radiation) was  
678 well validated against observations at more than 20 sites (Yue and Unger, 2018)(Yue  
679 and Unger, 2018). Such amelioration of GPP suggests that moderate aerosol loading is  
680 beneficial for ecosystem carbon uptake (Yue and Unger, 2017)(Yue and Unger, 2017).  
681 However, the dense aerosol loading may instead weaken plant photosynthesis due to  
682 the large reduction in direct radiation.

683

684 We further evaluate the ET responses to diffuse and direct radiation from the iMAPLE  
685 model (Figure 13g-13i). Although ET is slightly higher at the diffusive condition, the  
686 growth rates are weaker than that of GPP. The main cause of such difference is related



687 to the varied light dependence of ET components, which consist of canopy evaporation  
688 and transpiration. Transpiration is tightly coupled with photosynthesis and will increase  
689 by diffuse radiation at a similar rate. However, evaporation is more dependent on light  
690 quantity which will decrease with the extinction of aerosols. As a result, the weakened  
691 evaporation in part offsets the increased transpiration, leading to the smaller growth rate  
692 of ET than the responses of photosynthesis and the consequent enhancement in water  
693 use efficiency (Wang et al., 2023). The iMAPLE model reasonably captures the lower  
694 growth rates of ET than GPP in response to diffuse radiation at the selected sites.

Field Code Changed

695

696

Formatted: Font color: Auto

#### 697 **4. Conclusions and discussion**

698 We develop the iMAPLE model by coupling Noah-MP water module with YIBs  
699 vegetation model. Validations show that iMAPLE predicts reasonable distribution of  
700 soil moisture and soil temperature. Driven with these prognostic soil conditions and  
701 meteorology from reanalyses, the model reasonably reproduces the observed  
702 spatiotemporal variations of both GPP and ET fluxes at 201 sites and on the global scale.  
703 We further update the biogeochemical processes in iMAPLE to extend the model's  
704 capability in quantifying interactions between air pollution and land ecosystems. The  
705 model reasonably predicts wetland CH<sub>4</sub> emissions at 44 sites and yields the similar  
706 global map of CH<sub>4</sub> emissions compared to an ensemble of 13 biogeochemical models.  
707 In addition, predicted biomass burning and biogenic emissions are consistent with  
708 either satellite retrievals or results from other models. We assess the impacts of surface  
709 O<sub>3</sub> and aerosols on ecosystem fluxes. The LMA-based scheme links the O<sub>3</sub> sensitivity  
710 with vegetation LMA and predicts a global map of GPP loss that is consistent with the  
711 traditional scheme using the PFT-specific sensitivity. The updated scheme effectively  
712 reduces modeling uncertainties by decreasing the number of parameters for O<sub>3</sub>  
713 sensitivity and provides an option to apply the advanced LMA map from remote sensing.  
714 The model also reproduces the observed responses of GPP and ET to diffuse radiation  
715 with a lower growth rate for ET than GPP.

716

717 There are several limitations in the current version of iMAPLE model. First, it does not  
718 include the dynamic nutrient cycle. Although we implement the down regulation from  
719 Arora et al. (2009) to constrain CO<sub>2</sub> fertilization, this limitation is dependent only on  
720 the ambient CO<sub>2</sub> concentrations and could not represent the heterogeneous distribution  
721 of nutrients. As a result, the model could not reveal the biogeochemical effects of  
722 nitrogen and phosphorus deposition on land ecosystems. Second, the feedback of fire  
723 activities to ecosystems is ignored. The iMAPLE considers the impacts of fuel load on  
724 area burned at each modeling time step. However, these fire perturbations do not in turn  
725 change the vegetation distribution and composition. The vegetation model does not  
726 consider the competition among PFTs, so that fire perturbations are not allowed to  
727 change vegetation coverage. As a result, the interactions between fire and ecosystems  
728 are underestimated in the current model framework, potentially leading to  
729 overestimations of wildfire activity due to remaining fuel loads. Third, iMAPLE does  
730 not consider the dynamic changes in wetland area for CH<sub>4</sub> emissions. Although the  
731 Noah-MP module predicts runoff and underground water, the changes of hydrological  
732 cycles are not connected with wetland area in the model. Instead, a prescribed wetland  
733 dataset is applied to reduce the possible uncertainties but meanwhile ~~refrain~~limits the  
734 explorations of CH<sub>4</sub> changes in the historical and future periods. Meanwhile, iMAPLE  
735 model considers only dynamic soil water and temperature at 2-m level, which may  
736 influence the deeper soil interactions between climate and land terrestrial ecosystem  
737 especially for the drier conditions. These limitations will be the focuses of model  
738 development in the next step.

739

740 The iMAPLE model inherits the good capability of the original YIBs model in the  
741 simulations of carbon cycle. Furthermore, the iMAPLE upgrades the YIBs model with  
742 carbon-water coupling and more biogeochemical processes. With the iMAPLE model,  
743 we could assess the changes of carbon and water fluxes, as well as their coupling, in  
744 response to environmental perturbations (e.g., climate change, air pollution, land cover

745 change). Meanwhile, by coupling the iMAPLE with climate and/or chemical models,  
746 we could further quantify the changes of meteorology and atmospheric components in  
747 response to the biogeochemical and biogeophysical processes. For example, ~~Lei et al.~~  
748 ~~(2022)~~[Lei et al. \(2022\)](#) revealed the strong vegetation feedback to global surface O<sub>3</sub>  
749 during the drought periods using the YIBs model coupled to a chemical transport model.  
750 ~~Xie et al. (2019)~~[Xie et al. \(2019\)](#) found a significant increase in atmospheric CO<sub>2</sub>  
751 concentrations due to O<sub>3</sub>-induced vegetation damage using the YIBs model coupled  
752 with a regional climate-chemistry model. ~~Gong et al. (2021)~~[Gong et al. \(2021\)](#)  
753 estimated a surface warming in polluted regions due to the ozone-vegetation feedback  
754 using the YIBs model coupled with a global climate-chemistry model. These studies  
755 indicate that the iMAPLE model could be used either offline or online with other  
756 models to explore the interactions among climate, chemistry, and ecosystems.

757

758 *Acknowledgment.* This work was jointly supported by the National Key Research and  
759 Development Program of China (grant no. 2019YFA0606802), the National Natural  
760 Science Foundation of China (grant no. ~~42275128~~-[42275128](#)), and the [Natural Science](#)  
761 [Foundation of Jiangsu Province \(grant no. BK20220031\)](#).

762

763 *Author contributions.* XY,~~HL~~ designed the research and wrote the paper. XY, HaZ  
764 optimized codes, performed simulations, and analyzed results. ~~XY~~, HaZ, CT, YM, YH,  
765 CG implemented codes and collected data. HuZ helped with code implementations. All  
766 authors commented on and revised the manuscript.

767

768 *Competing interests.* The contact author has declared that none of the authors has any  
769 competing interests.

770

771 *Code availability.* The code for the iMAPLE version 1 model is available at  
772 <https://doi.org/10.6084/m9.figshare.23593578.v1>

773

774 *Data availability*. All the validation data are available to download from the cited  
775 references or data links shown in Section 2.4. The simulation data of monthly output  
776 from BASE experiment during 1980-2021 with the iMAPLE model are available at  
777 <https://doi.org/10.6084/m9.figshare.23593578.v1>

778

## 779 Reference

- 780 [Arora, V. K., Boer, G. J., Christian, J. R., Curry, C. L., Denman, K. L., Zahariev, K.,](#)  
781 [Flato, G. M., Scinocca, J. F., Merryfield, W. J., and Lee, W. G.: The Effect of](#)  
782 [Terrestrial Photosynthesis Down Regulation on the Twentieth-Century Carbon](#)  
783 [Budget Simulated with the CCCma Earth System Model, \*J Climate\*, 22, 6066-6088,](#)  
784 [10.1175/2009jcli3037.1, 2009.](#)
- 785 [Ball, J. T., Woodrow, I. E., and Berry, J. A.: A model predicting stomatal conductance](#)  
786 [and its contribution to the control of photosynthesis under different environmental](#)  
787 [conditions-~~in~~, in: \*Progress in Photosynthesis Research\*, edited by: Biggins, J.-\(Ed.\),](#)  
788 [Nijhoff, Dordrecht, Netherlands, 221-224, 1987.](#)
- 789 [Beer, C., Reichstein, M., Tomelleri, E., Ciais, P., Jung, M., Carvalhais, N., Rodenbeck,](#)  
790 [C., Arain, M. A., Baldocchi, D., Bonan, G. B., Bondeau, A., Cescatti, A., Lasslop,](#)  
791 [G., Lindroth, A., Lomas, M., Luysaert, S., Margolis, H., Oleson, K. W., Roupsard,](#)  
792 [O., Veenendaal, E., Viovy, N., Williams, C., Woodward, F. I., and Papale, D.:](#)  
793 [Terrestrial Gross Carbon Dioxide Uptake: Global Distribution and Covariation](#)  
794 [with Climate, \*Science\*, 329, 834-838, 10.1126/Science.1184984, 2010.](#)
- 795 [Cao, Y., Yue, X., Lei, Y., Zhou, H., Liao, H., Song, Y., Bai, J., Yang, Y., Chen, L., Zhu,](#)  
796 [J., Ma, Y., and Tian, C.: Identifying the drivers of modeling uncertainties in](#)  
797 [isoprene emissions: schemes versus meteorological forcings, \*Journal of\*](#)  
798 [Geophysical Research](#), 126, e2020JD034242, [10.1029/2020JD034242](#), 2021a.
- 799 [Cao, Y., Yue, X., Liao, H., Yang, Y., Zhu, J., Chen, L., Tian, C., Lei, Y., Zhou, H., and](#)  
800 [Ma, Y.: Ensemble projection of global isoprene emissions by the end of 21st](#)  
801 [century using CMIP6 models, \*Atmospheric Environment\*, 267, 118766,](#)  
802 [10.1016/j.atmosenv.2021.118766](#), 2021b.
- 803 [Carslaw, K. S., Boucher, O., Spracklen, D. V., Mann, G. W., Rae, J. G. L., Woodward,](#)  
804 [S., and Kulmala, M.: A review of natural aerosol interactions and feedbacks within](#)  
805 [the Earth system, \*Atmos Chem Phys\*, 10, 1701-1737, 10.5194/acp-10-1701-2010,](#)  
806 [2010.](#)
- 807 [Castillo, C. K. G., Levis, S., and Thornton, P.: Evaluation of the New CNDV Option of](#)  
808 [the Community Land Model: Effects of Dynamic Vegetation and Interactive](#)  
809 [Nitrogen on CLM4 Means and Variability, \*J Climate\*, 25, 3702-3714, 10.1175/Jcli-](#)  
810 [D-11-00372.1, 2012.](#)
- 811 [Chen, G., Guo, Y., Yue, X., Tong, S., Gasparri, A., Bell, M. L., Armstrong, B.,](#)  
812 [Schwartz, J., Jouni J K Jaakkola, Zanobetti, A., Lavigne, E., Saldiva, P. H. N., Kan,](#)  
813 [H., Royé, D., Milojevic, A., Overcenco, A., Urban, A., Schneider, A., Entezari, A.,](#)  
814 [Viciedo-Cabrera, A. M., Zeka, A., Tobias, A., Nunes, B., Alahmad, B., Bertil](#)

Formatted: Font: 小四

Formatted: Indent: Left: 0 cm, Hanging: 1.77 ch, First line: -1.77 ch

815 Forsberg, Pan, S.-C., Íñiguez, C., Ameling, C., Valencia, C. D. I. C., Åström, C.,  
816 Houthuijs, D., Dung, D. V., Samoli, E., Mayvaneh, F., Sera, F., Carrasco-Escobar,  
817 G., Lei, Y., Orru, H., Kim, H., Iulian-Horia Holobaca, Kysely, J., Teixeira, J. P.,  
818 Madureira, J., Katsouyanni, K., Hurtado-Díaz, M., Maasikmets, M., Ragetti, M.  
819 S., Hashizume, M., Stafoggia, M., Pascal, M., Scortichini, M., Micheline de Sousa  
820 Zanotti Stagliorio Coêlho, Ortega, N. V., Rytí, N. R. I., Scovronick, N., Matus, P.,  
821 Goodman, P., Garland, R. M., Abrutzky, R., Garcia, S. O., Rao, S., Fratianni, S.,  
822 Dang, T. N., Colistro, V., Huber, V., Lee, W., Seposo, X., Honda, Y., Guo, Y. L., Ye,  
823 T., Yu, W., Abramson, M. J., Samet, J. M., and Li, S.: Mortality risk attributable to  
824 wildfire-related PM<sub>2.5</sub> pollution: a global time series study in 749 locations, *The*  
825 *Lancet Planetary Health*, 5, e579-e587, [10.1016/S2542-5196\(21\)00200-X](https://doi.org/10.1016/S2542-5196(21)00200-X), 2021.

826 Clapp, R. B. and Hornberger, G. M.: Empirical equations for some soil hydraulic  
827 properties, *Water Resources Research*, 14, 601-604, 1978.

828 Cox, P. M.: Description of the "TRIFFID" Dynamic Global Vegetation Model, Hadley  
829 Centre technical note 24, Berks, UK, 2001.

830 Defries, R. S., Hansen, M. C., Townshend, J. R. G., Janetos, A. C., and Loveland, T. R.:  
831 A new global 1-km dataset of percentage tree cover derived from remote sensing,  
832 *Global Change Biology*, 6, 247-254, [10.1046/j.1365-2486.2000.00296.x](https://doi.org/10.1046/j.1365-2486.2000.00296.x), 2000.

833 Delwiche, K. B. and Knox, S. H. and Malhotra, A. and Fluet-Chouinard, E. and  
834 McNicol, G. and Feron, S. and Ouyang, Z. and Papale, D. and Trotta, C. and  
835 Canfora, E. and Cheah, Y. W. and Christianson, D. and Alberto, M. C. R. and  
836 Alekseychik, P. and Aurela, M. and Baldocchi, D. and Bansal, S. and Billesbach,  
837 D. P. and Bohrer, G. and Bracho, R. and Buchmann, N. and Campbell, D. I.  
838 and Celis, G. and Chen, J. and Chen, W. and Chu, H. and Dalmagro, H. J. and  
839 Dengel, S. and Desai, A. R. and Detto, M. and Dolman, H. and Eichelmann, E.  
840 and Euskirchen, E. and Famulari, D. and Fuchs, K. and Goeckede, M. and  
841 Gogo, S. and Gondwe, M. J. and Goodrich, J. P. and Gottschalk, P. and Graham,  
842 S. L. and Heimann, M. and Helbig, M. and Helfter, C. and Hemes, K. S. and  
843 Hirano, T. and Hollinger, D. and Hörtnagl, L. and Iwata, H. and Jacotot, A. and  
844 Jurasinski, G. and Kang, M. and Kasak, K. and King, J. and Klatt, J. and  
845 Koebisch, F. and Krauss, K. W. and Lai, D. Y. F. and Lohila, A. and Mammarella,  
846 I. and Belelli Marchesini, L. and Manca, G. and Matthes, J. H. and Maximov,  
847 T. and Merbold, L. and Mitra, B. and Morin, T. H. and Nemitz, E. and Nilsson,  
848 M. B. and Niu, S. and Oechel, W. C. and Oikawa, P. Y. and Ono, K. and Peichl,  
849 M. and Peltola, O. and Reba, M. L. and Richardson, A. D. and Riley, W. and  
850 Runkle, B. R. K. and Ryu, Y. and Sachs, T. and Sakabe, A. and Sanchez, C. R.  
851 and Schuur, E. A. and Schäfer, K. V. R. and Sonnentag, O. and Sparks, J. P. and  
852 Stuart-Haëntjens, E. and Sturtevant, C. and Sullivan, R. C. and Szutu, D. J. and  
853 Thom, J. E. and Torn, M. S. and Tuittila, E. S. and Turner, J. and Ueyama, M.  
854 and Valach, A. C. and Vargas, R. and Varlagin, A. and Vazquez-Lule, A. and  
855 Verfaillie, J. G. and Vesala, T. and Vourlitis, G. L. and Ward, E. J. and Wille, C.  
856 and Wohlfahrt, G. and Wong, G. X. and Zhang, Z. and Zona, D. and Windham-  
857 Myers, L. and Poulter, B. and Jackson, R. B.: FLUXNET-CH4: a global, multi-  
858 ecosystem dataset and analysis of methane seasonality from freshwater wetlands,

859 Earth Syst. Sci. Data, 13, 3607-3689, [10.5194/essd-13-3607-2021](https://doi.org/10.5194/essd-13-3607-2021), 2021.

860 Farquhar, G. D., Caemmerer, S. V., and Berry, J. A.: A ~~Biochemical Model~~biochemical-  
861 model of ~~Photosynthetic Co2 Assimilation~~photosynthetic CO2 assimilation in  
862 ~~Leaves~~leaves of C-3 ~~Species~~species, *Planta*, 149, 78-90, [10.1007/bf00386231](https://doi.org/10.1007/bf00386231), 1980.

863 ~~Friedlingstein, P. and O'Sullivan, M. and Jones, M. W. and Andrew, R. M. and Gregor, L. and~~  
864 ~~Hauck, J. and Quéré, C. L. and Luijkx, I. T. and Olsen, A. and Peters, G. P. and Peters, W.~~  
865 ~~and Pongratz, J. and Schwingshaeckl, C. and Sitch, S. and Canadell, J. G. and Ciais, P. and~~  
866 ~~Jackson, R. B. and Alin, S. R. and Alkama, R. and Arneth, A. and Arora, V. K. and Bates,~~  
867 ~~N. R. and Becker, M. and Bellouin, N. and Bittig, H. C. and Bopp, L. and Chevallier, F.~~  
868 ~~and Chini, L. P. and Cronin, M. and Decharme, B. and Evans, W. and Falk, S. and Feely,~~  
869 ~~R. A. and Gasser, T. and Gehlen, M. and Gkritzalis, T. and Gloege, L. and Grassi, G. and~~  
870 ~~Gruber, N. and Gürses, Ö. and Harris, I. and Hefner, M. and Houghton, R. A. and Hurtt,~~  
871 ~~G. C. and Iida, Y. and Ilyina, T. and Jain, A. K. and Jersild, A. and Kadono, K. and Kato,~~  
872 ~~E. and Kennedy, D. and Goldewijk, K. K. and Knauer, J. and Korsbakken, J. I. and~~  
873 ~~Landschützer, P. and Lefèvre, N. and Lindsay, K. and Liu, Z. and Liu, J. and Marland, G.~~  
874 ~~and Mayot, N. and McGrath, M. J. and Metzl, N. and Monacci, N. M. and Munro, D. R.~~  
875 ~~and Nakaoka, S. I. and Niwa, Y. and O'Brien, K. and Ono, T. and Palmer, P. I. and Pan, N.~~  
876 ~~and Pierrot, D. and Pocock, K. and Poulter, B. and Resplandy, L. and Robertson, E. and~~  
877 ~~Rödenbeck, C. and Rodriguez, C. and Rosan, T. M. and Schwinger, J. and Séférian, R. and~~  
878 ~~Shutler, J. D. and Skjelvan, I. and Steinhoff, T. and Sun, Q. and Sutton, A. J. and Sweeney,~~  
879 ~~C. and Takao, S. and Tanhua, T. and Tans, P. P. and Tian, X. and Tian, H. and Tilbrook, B.~~  
880 ~~and Tsujino, H. and Tubiello, F. and Werf, G. v. d. and Walker, A. P. and Wanninkhof, R.~~  
881 ~~and Whitehead, C. and Wranne, A. W. and Wright, R. and Yuan, W. and Yue, C. and Yue,~~  
882 ~~X. and Zaehle, S. and Zeng, J. and Zheng, B.: Global Carbon Budget 2022, Earth System~~  
883 ~~Science Data, 14, 4811-4900, 2022.~~

884 Friedlingstein, P., O'Sullivan, M., Jones, M. W., Andrew, R. M., Hauck, J., Olsen, A.,  
885 Peters, G. P., Peters, W., Pongratz, J., Sitch, S., Quéré, C. L., Canadell, J. G., Ciais,  
886 P. P., Jackson, R. B., Alin, S., Aragao, L. E., Arneth, A., Arora, V., Bates, N. R.,  
887 Becker, M., Benoit-Cattin, A., Bittig, H. C., Bopp, L., Bultan, S., Chandra, N.,  
888 Chevallier, F., Chini, L. P., Evans, W., Florentie, L., Forster, P. M., Gasser, T.,  
889 Gehlen, M., Gilfillan, D., Gkritzalis, T., Gregor, L., Gruber, N., Harris, I., Hartung,  
890 K., Haverd, V., Houghton, R. A., Ilyina, T., Jain, A. K., Joetzjer, E., Kadono, K.,  
891 Kato, E., Kitidis, V., Ivar, J. I. J., Landschützer, P., Lefèvre, N., Lenton, A., Lienert,  
892 S., Liu, Z., Lombardozi, D., Marland, G., Metzl, N., Munro, D. R., Nabel, J. E.,  
893 Nakaoka, S.-I., Niwa, Y., O'Brien, K., Ono, T., Palmer, P. I., Pierrot, D., Poulter,  
894 B., Resplandy, L., Robertson, E., Rödenbeck, C., Schwinger, J., Séférian, R.,  
895 Skjelvan, I., Smith, A. J., Sutton, A., Tanhua, T., Tans, P. P., Tian, H., Tilbrook, B.,  
896 Werf, G. R. v. d., Vuichard, N., Walker, A., Wanninkhof, R., Watson, A. J., Willis,  
897 D., Wiltshire, A. J., Yuan, W., Yue, X., and Zaehle, S.: Global Carbon Budget 2020,  
898 *Earth System Science Data*, 12, 3269-3340, 2020.

899 ~~Friedlingstein, P., O'Sullivan, M., Jones, M. W., Andrew, R. M., Gregor, L., Hauck, J.,~~  
900 ~~Quéré, C. L., Luijkx, I. T., Olsen, A., Peters, G. P., Peters, W., Pongratz, J.,~~  
901 ~~Schwingshaeckl, C., Sitch, S., Canadell, J. G., Ciais, P., Jackson, R. B., Alin, S. R.,~~  
902 ~~Alkama, R., Arneth, A., Arora, V. K., Bates, N. R., Becker, M., Bellouin, N., Bittig,~~

Formatted: Indent: Left: 0 cm, Hanging: 1.77 ch, First line: -1.77 ch

903 [H. C., Bopp, L., Chevallier, F., Chini, L. P., Cronin, M., Decharme, B., Evans, W.,](#)  
904 [Falk, S., Feely, R. A., Gasser, T., Gehlen, M., Gkritzalis, T., Gloege, L., Grassi, G.,](#)  
905 [Gruber, N., Gürses, Ö., Harris, I., Hefner, M., Houghton, R. A., Hurtt, G. C., Iida,](#)  
906 [Y., Ilyina, T., Jain, A. K., Jersild, A., Kadono, K., Kato, E., Kennedy, D., Goldewijk,](#)  
907 [K. K., Knauer, J., Korsbakken, J. I., Landschützer, P., Lefèvre, N., Lindsay, K., Liu,](#)  
908 [Z., Liu, J., Marland, G., Mayot, N., McGrath, M. J., Metzl, N., Monacci, N. M.,](#)  
909 [Munro, D. R., Nakaoka, S.-I., Niwa, Y., O'Brien, K., Ono, T., Palmer, P. I., Pan, N.,](#)  
910 [Pierrot, D., Pockock, K., Poulter, B., Resplandy, L., Robertson, E., Rödenbeck, C.,](#)  
911 [Rodriguez, C., Rosan, T. M., Schwinger, J., Séférian, R., Shutler, J. D., Skjelvan,](#)  
912 [I., Steinhoff, T., Sun, Q., Sutton, A. J., Sweeney, C., Takao, S., Tanhua, T., Tans, P.](#)  
913 [P., Tian, X., Tian, H., Tilbrook, B., Tsujino, H., Tubiello, F., Werf, G. v. d., Walker,](#)  
914 [A. P., Wanninkhof, R., Whitehead, C., Wranne, A. W., Wright, R., Yuan, W., Yue,](#)  
915 [C., Yue, X., Zaehle, S., Zeng, J., and Zheng, B.: Global Carbon Budget 2022. \*Earth\*](#)  
916 [System Science Data, 14, 4811-4900, 10.5194/essd-14-4811-2022, 2022.](#)

917 Gelaro, R., McCarty, W., Suarez, M. J., Todling, R., Molod, A., Takacs, L., Randles, C.  
918 A., Darmenov, A., Bosilovich, M. G., Reichle, R., Wargan, K., Coy, L., Cullather,  
919 R., Draper, C., Akella, S., Buchard, V., Conaty, A., da Silva, A. M., Gu, W., Kim,  
920 G. K., Koster, R., Lucchesi, R., Merkova, D., Nielsen, J. E., Partyka, G., Pawson,  
921 S., Putman, W., Rienecker, M., Schubert, S. D., Sienkiewicz, M., and Zhao, B.: The  
922 Modern-Era Retrospective Analysis for Research and Applications, Version 2  
923 (MERRA-2), *J Climate*, 30, 5419-5454, [10.1175/Jcli-D-16-0758.1](#), 2017.

924 Gong, C., Liao, H., Yue, X., Ma, Y., and Lei, Y.: Impacts of ozone-vegetation  
925 interactions on ozone pollution episodes in North China and the Yangtze River  
926 Delta, ~~*Geophys Res Lett*~~ *Geophysical Research Letters*, 48, e2021GL093814,  
927 [10.1029/2021GL093814](#), 2021.

928 Guenther, A. B., Jiang, X., Heald, C. L., Sakulyanontvittaya, T., Duhl, T., Emmons, L.  
929 K., and Wang, X.: The Model of Emissions of Gases and Aerosols from Nature  
930 version 2.1 (MEGAN2.1): an extended and updated framework for modeling  
931 biogenic emissions, *Geosci Model Dev*, 5, 1471-1492, [10.5194/Gmd-5-1471-2012](#),  
932 2012.

933 Hansen, M. C., DeFries, R. S., Townshend, J. R. G., Carroll, M., Dimiceli, C., and  
934 Sohlberg, R. A.: Global Percent Tree Cover at a Spatial Resolution of 500 Meters:  
935 First Results of the MODIS Vegetation Continuous Fields Algorithm, *Earth*  
936 *Interact*, 7, 1-15, ~~2003~~ [10.1175/1087-3562\(2003\)007<0001:GPTCAA>2.0.CO;2](#),  
937 [2003](#).

938 Heimann, I., Griffiths, P. T., Warwick, N. J., Abraham, N. L., Archibald, A. T., and Pyle,  
939 J. A.: Methane Emissions in a Chemistry-Climate Model: Feedbacks and Climate  
940 Response, *J Adv Model Earth Sy*, 12, e2019MS002019, [10.1029/2019MS002019](#),  
941 2020.

942 Hengl, T., de Jesus, J. M., Heuvelink, G. B. M., Gonzalez, M. R., Kilibarda, M.,  
943 Blagotic, A., Shangguan, W., Wright, M. N., Geng, X. Y., Bauer-Marschallinger,  
944 B., Guevara, M. A., Vargas, R., MacMillan, R. A., Batjes, N. H., Leenaars, J. G. B.,  
945 Ribeiro, E., Wheeler, I., Mantel, S., and Kempen, B.: SoilGrids250m: Global  
946 gridded soil information based on machine learning, *Plos One*, 12, ~~2017~~ [ARTN](#)

Formatted: Indent: Left: 0 cm, Hanging: 1.77 ch, First  
line: -1.77 ch



Formatted: Indent: Left: 0 cm, Hanging: 1.77 ch, First line: -1.77 ch

947 [e0169748](#)  
948 [10.1371/journal.pone.0169748.2017.](#)  
949 Jasechko, S., Sharp, Z. D., Gibson, J. J., Birks, S. J., Yi, Y., and Fawcett, P. J.: Terrestrial  
950 water fluxes dominated by transpiration, *Nature*, 496, 347-350,  
951 [10.1038/nature11983](#), 2013.  
952 Jung, M., Reichstein, M., Margolis, H. A., Cescatti, A., Richardson, A. D., Arain, M.  
953 A., Arneth, A., Bernhofer, C., Bonal, D., Chen, J. Q., Gianelle, D., Gobron, N.,  
954 Kiely, G., Kutsch, W., Lasslop, G., Law, B. E., Lindroth, A., Merbold, L.,  
955 Montagnani, L., Moors, E. J., Papale, D., Sottocornola, M., Vaccari, F., and  
956 Williams, C.: Global patterns of land-atmosphere fluxes of carbon dioxide, latent  
957 heat, and sensible heat derived from eddy covariance, satellite, and meteorological  
958 observations, *Journal of Geophysical Research*, 116, G00j07,  
959 [10.1029/2010jg001566](#), 2011.  
960 Jung, M., Schwalm, C., Migliavacca, M., Walther, S., Camps-Valls, G., Koirala, S.,  
961 Anthoni, P., Besnard, S., Bodesheim, P., Carvalhais, N., Chevallier, F., Gans, F.,  
962 Goll, D. S., Haverd, V., Köhler, P., Ichii, K., Jain, A. K., Liu, J., Lombardozi, D.,  
963 Nabel, J. E. M. S., Nelson, J. A., O'Sullivan, M., Pallandt, M., Papale, D., Peters,  
964 W., Pongratz, J., Rödenbeck, C., Sitch, S., Tramontana, G., Walker, A., Weber, U.,  
965 and Reichstein, M.: Scaling carbon fluxes from eddy covariance sites to globe:  
966 synthesis and evaluation of the FLUXCOM approach, *Biogeosciences*, 17, 1343-  
967 1365, [10.5194/bg-17-1343-2020](#), 2020a.  
968 Jung, M., Schwalm, C., Migliavacca, M., Walther, S., Camps-Valls, G., Koirala, S.,  
969 Anthoni, P., Besnard, S., Bodesheim, P., Carvalhais, N., Chevallier, F., Gans, F.,  
970 Goll, D. S., Haverd, V., Kohler, P., Ichii, K., Jain, A. K., Liu, J. Z., Lombardozi,  
971 D., Nabel, J. E. M. S., Nelson, J. A., O'Sullivan, M., Pallandt, M., Papale, D., Peters,  
972 W., Pongratz, J., Rodenbeck, C., Sitch, S., Tramontana, G., Walker, A., Weber, U.,  
973 and Reichstein, M.: Scaling carbon fluxes from eddy covariance sites to globe:  
974 synthesis and evaluation of the FLUXCOM approach, *Biogeosciences*, 17, 1343-  
975 1365, [10.5194/bg-17-1343-2020](#), 2020b.  
976 Kattge, J.-and., Diaz, S.-and., Lavorel, S.-and., Prentice, C.-and., Leadley, P.-and., Bonisch,  
977 G.-and., Garnier, E.-and., Westoby, M.-and., Reich, P. B.-and., Wright, I. J.-and.,  
978 Cornelissen, J. H. C.-and., Violle, C.-and., Harrison, S. P.-and., van Bodegom, P. M.-  
979 and., Reichstein, M.-and., Enquist, B. J.-and., Soudzilovskaia, N. A.-and., Ackerly,  
980 D. D.-and., Anand, M.-and., Atkin, O.-and., Bahn, M.-and., Baker, T. R.-and.,  
981 Baldocchi, D.-and., Bekker, R.-and., Blanco, C. C.-and., Blonder, B.-and., Bond, W.  
982 J.-and., Bradstock, R.-and., Bunker, D. E.-and., Casanoves, F.-and., Cavender-Bares,  
983 J.-and., Chambers, J. Q.-and., Chapin, F. S.-and., Chave, J.-and., Coomes, D.-and.,  
984 Cornwell, W. K.-and., Craine, J. M.-and., Dobrin, B. H.-and., Duarte, L.-and., Durka,  
985 W.-and., Elser, J.-and., Esser, G.-and., Estiarte, M.-and., Fagan, W. F.-and., Fang, J.-  
986 and., Fernandez-Mendez, F.-and., Fidelis, A.-and., Finegan, B.-and., Flores, O.-and.,  
987 Ford, H.-and., Frank, D.-and., Freschet, G. T.-and., Fyllas, N. M.-and., Gallagher, R.  
988 V.-and., Green, W. A.-and., Gutierrez, A. G.-and., Hickler, T.-and., Higgins, S. I.-and.,  
989 Hodgson, J. G.-and., Jalili, A.-and., Jansen, S.-and., Joly, C. A.-and., Kerckhoff, A. J.-  
990 and., Kirkup, D.-and., Kitajima, K.-and., Kleyer, M.-and., Klotz, S.-and., Knops, J.



991 M. H.-and., Kramer, K.-and., Kuhn, I.-and., Kurokawa, H.-and., Laughlin, D.-and.,  
992 Lee, T. D.-and., Leishman, M.-and., Lens, F.-and., Lenz, T.-and., Lewis, S. L.-and.,  
993 Lloyd, J.-and., Llusia, J.-and., Louault, F.-and., Ma, S.-and., Mahecha, M. D.-and.,  
994 Manning, P.-and., Massad, T.-and., Medlyn, B. E.-and., Messier, J.-and., Moles, A.  
995 T.-and., Muller, S. C.-and., Nadrowski, K.-and., Naeem, S.-and., Niinemets, U.-and.,  
996 Nollert, S.-and., Nuske, A.-and., Ogaya, R.-and., Oleksyn, J.-and., Onipchenko, V. G.-  
997 and., Onoda, Y.-and., Ordonez, J.-and., Overbeck, G.-and., Ozinga, W. A.-and., Patino,  
998 S.-and., Paula, S.-and., Pausas, J. G.-and., Penuelas, J.-and., Phillips, O. L.-and., Pillar,  
999 V.-and., Poorter, H.-and., Poorter, L.-and., Poschlod, P.-and., Prinzing, A.-and., Proulx,  
1000 R.-and., Rammig, A.-and., Reinsch, S.-and., Reu, B.-and., Sack, L.-and., Salgado-  
1001 Negre, B.-and., Sardans, J.-and., Shiodera, S.-and., Shipley, B.-and., Siefert, A.-and.,  
1002 Sosinski, E.-and., Soussana, J. F.-and., Swaine, E.-and., Swenson, N.-and., Thompson,  
1003 K.-and., Thornton, P.-and., Waldram, M.-and., Weiher, E.-and., White, M.-and., White,  
1004 S.-and., Wright, S. J.-and., Yguel, B.-and., Zaehle, S.-and., Zanne, A. E., and Wirth,  
1005 C.: TRY - a global database of plant traits, *Global Change Biology*, 17, 2905-2935,  
1006 [10.1111/j.1365-2486.2011.02451.x](https://doi.org/10.1111/j.1365-2486.2011.02451.x), 2011.

1007 Keeling, C. D., Bacastow, R. B., Bainbridge, A. E., Ekdahl, C. A., Guenther, P. R.,  
1008 Waterman, L. S., and Chin, J. F. S.: Atmospheric carbon dioxide variations at  
1009 Mauna Loa Observatory, Hawaii, *Tellus A.*, 28, 538-551, [1976-10.1111/j.2153-  
1010 3490.1976.tb00701.x](https://doi.org/10.1111/j.2153-3490.1976.tb00701.x), 1976.

1011 Lei, Y., Yue, X., Liao, H., Gong, C., and Zhang, L.: Implementation of Yale Interactive  
1012 terrestrial Biosphere model v1.0 into GEOS-Chem v12.0.0: a tool for biosphere-  
1013 chemistry interactions, *Geosci Model Dev*, 13, 1137-1153, [10.5194/gmd-13-1137-  
1014 2020](https://doi.org/10.5194/gmd-13-1137-2020), 2020.

1015 Lei, Y., Yue, X., Liao, H., Zhang, L., Zhou, H., Tian, C., Gong, C., Ma, Y., Cao, Y., Seco,  
1016 R., Karl, T., and Potosnak, M.: Global perspective of drought impacts on ozone  
1017 pollution episodes, *Environmental Science & Technology*, 56, 3932-3940, 2022.

1018 Li, F., Zeng, X. D., and Levis, S.: A process-based fire parameterization of intermediate  
1019 complexity in a Dynamic Global Vegetation Model (vol 9, pg 2761, 2012),  
1020 *Biogeosciences*, 9, 4771-4772, [10.5194/bg-9-4771-2012](https://doi.org/10.5194/bg-9-4771-2012), 2012.

1021 Li, X., and Xiao, J.: Mapping Photosynthesis Solely from Solar-Induced Chlorophyll  
1022 Fluorescence: A Global, Fine-Resolution Dataset of Gross Primary Production  
1023 Derived from OCO-2, *Remote Sensing*, 11, 2563, [10.3390/rs11212563](https://doi.org/10.3390/rs11212563), 2019.

1024 Lin, M. Y., Horowitz, L. W., Xie, Y. Y., Paulot, F., Malyshev, S., Shevliakova, E., Finco,  
1025 A., Gerosa, G., Kubistin, D., and Pilegaard, K.: Vegetation feedbacks during  
1026 drought exacerbate ozone air pollution extremes in Europe, *Nat Clim Change*, 10,  
1027 444-451, [10.1038/s41558-020-0743-y](https://doi.org/10.1038/s41558-020-0743-y), 2020.

1028 Lombardozzi, D., Levis, S., Bonan, G., Hess, P. G., and Sparks, J. P.: The Influence of  
1029 Chronic Ozone Exposure on Global Carbon and Water Cycles, *J Climate*, 28, 292-  
1030 305, [10.1175/Jcli-D-14-00223.1](https://doi.org/10.1175/Jcli-D-14-00223.1), 2015.

1031 [Ma, Y., Yue, X., Zhou, H., Gong, C., Lei, Y., Tian, C., and Cao, Y.: Identifying the  
1032 dominant climate-driven uncertainties in modeling gross primary productivity,  
1033 \*Science of the Total Environment\*, 800, 149518, \[10.1016/j.scitotenv.2021.149518\]\(https://doi.org/10.1016/j.scitotenv.2021.149518\),  
1034 \[2021\]\(https://doi.org/10.1016/j.scitotenv.2021.149518\).](https://doi.org/10.1016/j.scitotenv.2021.149518)

1035 Ma, Y., Yue, X., Sitch, S., Unger, N., Uddling, J., Mercado, L. M., Gong, C., Feng, Z.,  
 1036 Yang, H., Zhou, H., Tian, C., Cao, Y., Lei, Y., Cheesman, A. W., Xu, Y., and Rojas,  
 1037 M. C. D.: Implementation of trait-based ozone plant sensitivity in the Yale  
 1038 Interactive terrestrial Biosphere model v1.0 to assess global vegetation damage,  
 1039 Geosci Model Dev, 16, 2261-2276, [10.5194/gmd-16-2261-2023](https://doi.org/10.5194/gmd-16-2261-2023), 2023.

~~1040 Ma, Y., Yue, X., Zhou, H., Gong, C., Lei, Y., Tian, C., and Cao, Y.: Identifying the  
 1041 dominant climate-driven uncertainties in modeling gross primary productivity,  
 1042 Science of the Total Environment, 800, 149518, 2021.~~

1043 Madani, N., Kimball, J. S., and Running, S. W.: Improving Global Gross Primary  
 1044 Productivity Estimates by Computing Optimum Light Use Efficiencies Using Flux  
 1045 Tower Data, Journal of Geophysical Research-Biogeosciences, 122, 2939-2951,  
 1046 [10.1002/2017jg004142](https://doi.org/10.1002/2017jg004142), 2017.

1047 Mercado, L. M., Bellouin, N., Sitch, S., Boucher, O., Huntingford, C., Wild, M., and  
 1048 Cox, P. M.: Impact of changes in diffuse radiation on the global land carbon sink,  
 1049 Nature, 458, 1014-U1087, [10.1038/Nature07949](https://doi.org/10.1038/Nature07949), 2009.

1050 Moreno-Martínez, Á., Camps-Valls, G., Kattge, J., Robinson, N., Reichstein, M.,  
 1051 Bodegom, P. V., and Running, S. W.: Global maps of leaf traits at 3km resolution,  
 1052 TRY File Archive, [in](https://trypal.org/), 2018.

1053 Niu, G. Y., Yang, Z. L., Mitchell, K. E., Chen, F., Ek, M. B., Barlage, M., Kumar, A.,  
 1054 Manning, K., Niyogi, D., Rosero, E., Tewari, M., and Xia, Y. L.: The community  
 1055 Noah land surface model with multiparameterization options (Noah-MP): 1. Model  
 1056 description and evaluation with local-scale measurements, Journal of Geophysical  
 1057 Research, 116, D12109, [10.1029/2010jd015139](https://doi.org/10.1029/2010jd015139), 2011.

1058 Paudel, R., Mahowald, N. M., Hess, P. G. M., Meng, L., and Riley, W. J.: Attribution  
 1059 of changes in global wetland methane emissions from pre-industrial to present  
 1060 using CLM4.5-BGC, Environ Res Lett, 11, 034020, [10.1088/1748-  
 1061 9326/11/3/034020](https://doi.org/10.1088/1748-9326/11/3/034020), 2016.

1062 Pechony, O., and Shindell, D. T.: Fire parameterization on a global scale, Journal of  
 1063 Geophysical Research-Atmospheres, 114, D16115, [10.1029/2009jd011927](https://doi.org/10.1029/2009jd011927), 2009.

1064 Piao, S. L., Ciais, P., Friedlingstein, P., de Noblet-Ducoudre, N., Cadule, P., Viovy, N.,  
 1065 and Wang, T.: Spatiotemporal patterns of terrestrial carbon cycle during the 20th  
 1066 century, Global Biogeochem Cy, 23, Gb4026, [10.1029/2008gb003339](https://doi.org/10.1029/2008gb003339), 2009.

1067 Randerson, J. T., Chen, Y., van der Werf, G. R., Rogers, B. M., and Morton, D. C.:  
 1068 Global burned area and biomass burning emissions from small fires, Journal of  
 1069 Geophysical Research-Biogeosciences, 117, G04012, [10.1029/2012jg002128](https://doi.org/10.1029/2012jg002128),  
 1070 2012.

1071 Rap, A., Scott, C. E., Reddington, C. L., Mercado, L., Ellis, R. J., Garraway, S., Evans,  
 1072 M. J., Beerling, D. J., MacKenzie, A. R., Hewitt, C. N., and Spracklen, D. V.:  
 1073 Enhanced global primary production by biogenic aerosol via diffuse radiation  
 1074 fertilization, Nat Geosci, 11, 640-644, [10.1038/s41561-018-0208-3](https://doi.org/10.1038/s41561-018-0208-3), 2018.

1075 Rosentreter, J. A., Borges, A. V., Deemer, B. R., Holgerson, M. A., Liu, S. D., Song, C.  
 1076 L., Melack, J., Raymond, P. A., Duarte, C. M., Allen, G. H., Olefeldt, D., Poulter,  
 1077 B., Battin, T. I., and Eyre, B. D.: Half of global methane emissions come from  
 1078 highly variable aquatic ecosystem sources, Nature Geoscience, 14, 225-+,

Formatted: Indent: Left: 0 cm, Hanging: 1.77 ch, First line: -1.77 ch

Formatted: Indent: Left: 0 cm, Hanging: 1.77 ch, First line: -1.77 ch

1079 [10.1038/s41561-021-00715-2](https://doi.org/10.1038/s41561-021-00715-2), 2021.

1080 Running, S., Nemani, R., Heinsch, F., Zhao, M., Reeves, M., and Hashimoto, H.: A  
1081 continuous satellite-derived measure of global terrestrial primary production,  
1082 *BioScience*, 54, 547-560, [2004.10.1641/0006-  
1083 3568\(2004\)054\[0547:ACSMOG\]2.0.CO;2, 2004.](https://doi.org/2004.10.1641/0006-3568(2004)054[0547:ACSMOG]2.0.CO;2)

1084 Saunois, M., Stavert, A. R., Poulter, B., Bousquet, P., Canadell, J. G., Jackson, R. B.,  
1085 Raymond, P. A., Dlugokencky, E. J., Houweling, S., Patra, P. K., Ciais, P., Arora,  
1086 V. K., Bastviken, D., Bergamaschi, P., Blake, D. R., Brailsford, G., Bruhwiler, L.,  
1087 Carlson, K. M., Carrol, M., Castaldi, S., Chandra, N., Crevoisier, C., Crill, P. M.,  
1088 Covey, K., Curry, C. L., Etiope, G., Frankenberg, C., Gedney, N., Hegglin, M. I.,  
1089 Hoglund-Isaksson, L., Hugelius, G., Ishizawa, M., Ito, A., Janssens-Maenhout, G.,  
1090 Jensen, K. M., Joos, F., Kleinen, T., Krummel, P. B., Langenfelds, R. L., Laruelle,  
1091 G. G., Liu, L. C., Machida, T., Maksyutov, S., McDonald, K. C., McNorton, J.,  
1092 Miller, P. A., Melton, J. R., Morino, I., Muller, J., Murguia-Flores, F., Naik, V.,  
1093 Niwa, Y., Noce, S., Doherty, S. O., Parker, R. J., Peng, C. H., Peng, S. S., Peters,  
1094 G. P., Prigent, C., Prinn, R., Ramonet, M., Regnier, P., Riley, W. J., Rosentreter, J.  
1095 A., Segers, A., Simpson, I. J., Shi, H., Smith, S. J., Steele, L. P., Thornton, B. F.,  
1096 Tian, H. Q., Tohjima, Y., Tubiello, F. N., Tsuruta, A., Viovy, N., Voulgarakis, A.,  
1097 Weber, T. S., van Weele, M., van der Werf, G. R., Weiss, R. F., Worthy, D., Wunch,  
1098 D., Yin, Y., Yoshida, Y., Zhang, W. X., Zhang, Z., Zhao, Y. H., Zheng, B., Zhu, Q.,  
1099 Zhu, Q. A., and Zhuang, Q. L.: The Global Methane Budget 2000-2017, *Earth  
1100 System Science Data*, 12, 1561-1623, [10.5194/essd-12-1561-2020](https://doi.org/10.5194/essd-12-1561-2020), 2020.

1101 Schaake, J. C., Koren, V. I., Duan, Q.-Y., Mitchell, K., and Chen, F.: Simple water  
1102 balance model for estimating runoff at different spatial and temporal scales, *Journal  
1103 of Geophysical Research*, 101, 7461-7475, [10.1029/95JD02892](https://doi.org/10.1029/95JD02892), 1996.

1104 Schaefer, K., Collatz, G. J., Tans, P., Denning, A. S., Baker, I., Berry, J., Prihodko, L.,  
1105 Suits, N., and Philpott, A.: Combined Simple Biosphere/Carnegie-Ames-Stanford  
1106 Approach terrestrial carbon cycle model, *J Geophys Res-Bioge*, 113, G03034,  
1107 [10.1029/2007jg000603](https://doi.org/10.1029/2007jg000603), 2008.

1108 Scholes, R. J., Colstoun, E. B. d., Hall, F. G., Collatz, G. J., Meeson, B. W., Los, S. O.,  
1109 and Landis, D. R.: ISLSCP II Global Gridded Soil Characteristics-, [in](https://doi.org/10.1029/2007jg000603), ORNL  
1110 DAAC, Oak Ridge, Tennessee, USA, 2011.

1111 Sitch, S., Cox, P. M., Collins, W. J., and Huntingford, C.: Indirect radiative forcing of  
1112 climate change through ozone effects on the land-carbon sink, *Nature*, 448, 791-  
1113 ~~794~~[U794, 10.1038/nature06059](https://doi.org/10.1038/nature06059), 2007.

1114 Sitch, S., Friedlingstein, P., Gruber, N., Jones, S. D., Murray-Tortarolo, G., Ahlström,  
1115 A., Doney, S. C., Graven, H., Heinze, C., Huntingford, C., Levis, S., Levy, P. E.,  
1116 Lomas, M., Poulter, B., Viovy, N., Zaehle, S., Zeng, N., Arneeth, A., Bonan, G.,  
1117 Bopp, L., Canadell, J. G., Chevallier, F., Ciais, P., Ellis, R., Gloor, M., Peylin, P.,  
1118 Piao, S. L., Quéré, C. L., Smith, B., Zhu, Z., and Myneni, R.: Recent trends and  
1119 drivers of regional sources and sinks of carbon dioxide, *Biogeosciences*, 12, 653-  
1120 679, 2015.

1121 Spitters, C. J. T.: Separating the Diffuse and Direct Component of Global Radiation and  
1122 Its Implications for Modeling Canopy Photosynthesis .2. Calculation of Canopy

1123       Photosynthesis, *Agr Forest Meteorol*, 38, 231-242, [10.1016/0168-1923\(86\)90061-](https://doi.org/10.1016/0168-1923(86)90061-4)  
1124 [4](https://doi.org/10.1016/0168-1923(86)90061-4), 1986.

1125 Spracklen, D. V., Arnold, S. R., and Taylor, C. M.: Observations of increased tropical  
1126 rainfall preceded by air passage over forests, *Nature*, 489, 282-U127, 2012.

1127 Terrer, C., Jackson, R. B., Prentice, I. C., Keenan, T. F., Kaiser, C., Vicca, S., Fisher, J.  
1128 B., Reich, P. B., Stocker, B. D., Hungate, B. A., Penuelas, J., McCallum, I.,  
1129 Soudzilovskaia, N. A., Cernusak, L. A., Talhelm, A. F., Van Sundert, K., Piao, S.  
1130 L., Newton, P. C. D., Hovenden, M. J., Blumenthal, D. M., Liu, Y. Y., Muller, C.,  
1131 Winter, K., Field, C. B., Viechtbauer, W., Van Lissa, C. J., Hoosbeek, M. R.,  
1132 Watanabe, M., Koike, T., Leshyk, V. O., Polley, H. W., and Franklin, O.: Nitrogen  
1133 and phosphorus constrain the CO<sub>2</sub> fertilization of global plant biomass, *Nat Clim*  
1134 *Change*, 9, 684-689, [10.1038/s41558-019-0545-2](https://doi.org/10.1038/s41558-019-0545-2), 2019.

1135 ~~Tian, C., Yue, X., Zhu, J., Liao, H., Yang, Y., Lei, Y., Zhou, X., Zhou, H., Ma, Y., and~~  
1136 ~~Cao, Y.: Fire-climate interactions through aerosol radiative effect in a global~~  
1137 ~~chemistry-climate-vegetation model, *Atmospheric Chemistry and Physics*, 22,~~  
1138 ~~[12353-12366](https://doi.org/10.5194/acp-22-12353-2022), [10.5194/acp-22-12353-2022](https://doi.org/10.5194/acp-22-12353-2022), 2022.~~

1139 Tian, C., Yue, X., Zhu, J., Liao, H., Yang, Y., Chen, L., Zhou, X., Lei, Y., Zhou, H., and  
1140 Cao, Y.: Projections of fire emissions and the consequent impacts on air quality  
1141 under 1.5°C and 2°C global warming, *Environmental Pollution/Environ Pollut*, 323,  
1142 [121311](https://doi.org/10.1016/j.envpol.2023.121311), [10.1016/j.envpol.2023.121311](https://doi.org/10.1016/j.envpol.2023.121311), 2023.

1143 ~~Tian, C., Yue, X., Zhu, J., Liao, H., Yang, Y., Lei, Y., Zhou, X., Zhou, H., Ma, Y., and~~  
1144 ~~Cao, Y.: Fire-climate interactions through aerosol radiative effect in a global~~  
1145 ~~chemistry-climate-vegetation model, *Atmos Chem Phys*, 22, 12353-12366, 2022.~~

1146 Unger, N., Harper, K., Zheng, Y., Kiang, N. Y., Aleinov, I., Arneth, A., Schurgers, G.,  
1147 Amelynck, C., Goldstein, A., Guenther, A., Heinesch, B., Hewitt, C. N., Karl, T.,  
1148 Laffineur, Q., Langford, B., McKinney, K. A., Misztal, P., Potosnak, M., Rinne, J.,  
1149 Pressley, S., Schoon, N., and Serça, D.: Photosynthesis-dependent isoprene  
1150 emission from leaf to planet in a global carbon–chemistry–climate model, *Atmos.*  
1151 *Chem. Phys.*, 13, 10243-10269, [10.5194/acp-13-10243-2013](https://doi.org/10.5194/acp-13-10243-2013), 2013.

1152 van der Werf, G. R., Randerson, J. T., Giglio, L., Collatz, G. J., Mu, M., Kasibhatla, P.  
1153 S., Morton, D. C., DeFries, R. S., Jin, Y., and van Leeuwen, T. T.: Global fire  
1154 emissions and the contribution of deforestation, savanna, forest, agricultural, and  
1155 peat fires (1997-2009), *Atmos Chem Phys*, 10, 11707-11735, [10.5194/Acp-10-](https://doi.org/10.5194/Acp-10-11707-2010)  
1156 [11707-2010](https://doi.org/10.5194/Acp-10-11707-2010), 2010.

1157 Walter, B. P., and Heimann, M.: A process-based, climate-sensitive model to derive  
1158 methane emissions from natural wetlands: Application to five wetland sites,  
1159 sensitivity to model parameters, and climate, *Global Biogeochem Cy*, 14, 745-765,  
1160 [10.1029/1999GB001204](https://doi.org/10.1029/1999GB001204), 2000.

1161 Walter, B. P., Heimann, M., and Matthews, E.: Modeling modern methane emissions  
1162 from natural wetlands: I. Model description and results, *Journal of Geophysical*  
1163 *Research*, 106, 34189-34206, [10.1029/2001JD900165](https://doi.org/10.1029/2001JD900165), 2001.

1164 Wang, B., Yue, X., Zhou, H., Lu, X., and Zhu, J.: Enhanced ecosystem water-use  
1165 efficiency under the more diffuse radiation conditions, *Global Biogeochem*

Formatted: Indent: Left: 0 cm, Hanging: 1.77 ch, First line: -1.77 ch

Formatted: Indent: Left: 0 cm, Hanging: 1.77 ch, First line: -1.77 ch

- 1166 [CyBiogeochemical Cycles](#), 37, e2022GB007606, [10.1029/2022GB007606](#), 2023.
- 1167 Wang, S. H., Zhang, Y. G., Ju, W. M., Chen, J. M., Ciais, P., Cescatti, A., Sardans, J.,  
1168 Janssens, I. A., Wu, M. S., Berry, J. A., Campbell, E., Fernandez-Martinez, M.,  
1169 Alkama, R., Sftch, S., Friedlingstein, P., Smith, W. K., Yuan, W. P., He, W.,  
1170 Lombardozzi, D., Kautz, M., Zhu, D., Lienert, S., Kato, E., Poulter, B., Sanders, T.  
1171 G. M., Kruger, I., Wang, R., Zeng, N., Tian, H. Q., Vuichard, N., Jain, A. K.,  
1172 Wiltshire, A., Haverd, V., Goll, D. S., and Penuelas, J.: Recent global decline of  
1173 CO<sub>2</sub> fertilization effects on vegetation photosynthesis, *Science*, 370, 1295-1300,  
1174 [10.1126/science.abb7772](#), 2020.
- 1175 Wania, R., Ross, I., and Prentice, I. C.: Implementation and evaluation of a new  
1176 methane model within a dynamic global vegetation model: LPJ-WHyMe v1.3.1,  
1177 *Geosci Model Dev*, 3, 565-584, [10.5194/gmd-3-565-2010](#), 2010.
- 1178 Warneke, C., Schwarz, J. P., Dibb, J., Kalashnikova, O., Frost, G., Al-Saad, J., Brown,  
1179 S. S., Brewer, W. A., Soja, A., Seidel, F. C., Washenfelder, R. A., Wiggins, E. B.,  
1180 Moore, R. H., Anderson, B. E., Jordan, C., Yacovitch, T. I., Herndon, S. C., Liu, S.,  
1181 Kuwayama, T., Jaffe, D., Johnston, N., Selimovic, V., Yokelson, R., Giles, D. M.,  
1182 Holben, B. N., Goloub, P., Popovici, I., Trainer, M., Kumar, A., Pierce, R. B., Fahey,  
1183 D., Roberts, J., Gargulinski, E. M., Peterson, D. A., Ye, X. X., Thapa, L. H., Saide,  
1184 P. E., Fite, C. H., Holmes, C. D., Wang, S. Y., Coggon, M. M., Decker, Z. C. J.,  
1185 Stockwell, C. E., Xu, L., Gkatzelis, G., Aikin, K., Lefer, B., Kaspari, J., Griffin, D.,  
1186 Zeng, L. H., Weber, R., Hastings, M., Chai, J. J., Wolfe, G. M., Hanisco, T. F., Liao,  
1187 J., Jost, P. C., Guo, H. Y., Jimenez, J. L., Crawford, J., and Team, F.-A. S.: Fire  
1188 Influence on Regional to Global Environments and Air Quality (FIREX-AQ),  
1189 *Journal of Geophysical Research*, 128, e2022JD037758, [10.1029/2022JD037758](#),  
1190 2023.
- 1191 Worden, J., Saatchi, S., Keller, M., Bloom, A. A., Liu, J., Parazoo, N., Fisher, J. B.,  
1192 Bowman, K., Reager, J. T., Fahy, K., Schimel, D., Fu, R., Worden, S., Yin, Y.,  
1193 Gentine, P., Konings, A. G., Quetin, G. R., Williams, M., Worden, H., Shi, M. J.,  
1194 and Barkhordarian, A.: Satellite Observations of the Tropical Terrestrial Carbon  
1195 Balance and Interactions With the Water Cycle During the 21st Century, *Rev*  
1196 *Geophys*, 59, e2020RG000711, [10.1029/2020RG000711](#), 2021.
- 1197 Wu, K., Yang, X. Y., Chen, D., Gu, S., Lu, Y. Q., Jiang, Q., Wang, K., Ou, Y. H., Qian,  
1198 Y., Shao, P., and Lu, S. H.: Estimation of biogenic VOC emissions and their  
1199 corresponding impact on ozone and secondary organic aerosol formation in China,  
1200 *Atmos Res*, 231, 104656, [10.1016/j.atmosres.2019.104656](#), 2020.
- 1201 Xie, X., Wang, T., Yue, X., Li, S., Zhuang, B., Wang, M., and Yang, X.: Numerical  
1202 modeling of ozone damage to plants and its effects on atmospheric CO<sub>2</sub> in China,  
1203 *Atmospheric Environment*, 217, 116970, [10.1016/j.atmosenv.2019.116970](#), 2019.
- 1204 Yuan, W. P., Liu, S. G., Yu, G. R., Bonnefond, J. M., Chen, J. Q., Davis, K., Desai, A.  
1205 R., Goldstein, A. H., Gianelle, D., Rossi, F., Suyker, A. E., and Verma, S. B.: Global  
1206 estimates of evapotranspiration and gross primary production based on MODIS  
1207 and global meteorology data, *Remote Sensing of Environment*, 114, 1416-1431,  
1208 2010.
- 1209 Yuan, X. Y., Calatayud, V., Gao, F., Fares, S., Paoletti, E., Tian, Y., and Feng, Z. Z.:

1210 Interaction of drought and ozone exposure on isoprene emission from extensively  
 1211 cultivated poplar, *Plant Cell Environ*, 39, 2276-2287, [10.1111/pce.12798](https://doi.org/10.1111/pce.12798), 2016.

1212 ~~Yue, X., Keenan, T. F., Munger, W., and Unger, N.: Limited effect of ozone reductions~~  
 1213 ~~on the 20-year photosynthesis trend at Harvard forest, *Global Change Biology*, 22,~~  
 1214 ~~3750-3759, 2016.~~

1215 ~~Yue, X. and Unger, N.: Aerosol optical depth thresholds as a tool to assess diffuse radiation~~  
 1216 ~~fertilization of the land carbon uptake in China, *Atmos Chem Phys*, 17, 1329-1342, 2017.~~

1217 ~~Yue, X. and Unger, N.: Fire air pollution reduces global terrestrial productivity, *Nature*~~  
 1218 ~~*Communications*, 9, 5413, 2018.~~

1219 ~~Yue, X., Yue, X., and Unger, N.: Ozone vegetation damage effects on gross primary~~  
 1220 ~~productivity in the United States, *Atmos Chem Phys* *Atmospheric Chemistry and*~~  
 1221 ~~*Physics*, 14, 9137-9153, [10.5194/acp-14-9137-2014](https://doi.org/10.5194/acp-14-9137-2014), 2014.~~

1222 Yue, X., and Unger, N.: The Yale Interactive terrestrial Biosphere model version 1.0:  
 1223 description, evaluation and implementation into NASA GISS ModelE2, *Geosci*  
 1224 *Model Dev*, 8, 2399-2417, [10.5194/gmd-8-2399-2015](https://doi.org/10.5194/gmd-8-2399-2015), 2015.

1225 ~~Yue, X., Unger, N., Harper, K., Xia, X., Liao, H., Zhu, T., Xiao, J., Feng, Z., and Li, J.:~~  
 1226 ~~Ozone and haze pollution weakens net primary productivity in China, *Atmos Chem Phys*,~~  
 1227 ~~17, 6073-6089, 2017.~~

1228 Yue, X., Unger, N., Keenan, T. F., Zhang, X., and Vogel, C. S.: Probing the past 30-year  
 1229 phenology trend of U.S. deciduous forests, *Biogeosciences*, 12, 4693-4709,  
 1230 [10.5194/bg-12-4693-2015](https://doi.org/10.5194/bg-12-4693-2015), 2015.

1231 ~~Yue, X., Keenan, T. F., Munger, W., and Unger, N.: Limited effect of ozone reductions~~  
 1232 ~~on the 20-year photosynthesis trend at Harvard forest, *Global Change Biology*, 22,~~  
 1233 ~~3750-3759, [10.1111/gcb.13300](https://doi.org/10.1111/gcb.13300), 2016.~~

1234 ~~Yue, X., and Unger, N.: Aerosol optical depth thresholds as a tool to assess diffuse~~  
 1235 ~~radiation fertilization of the land carbon uptake in China, *Atmospheric Chemistry*~~  
 1236 ~~*and Physics*, 17, 1329-1342, [10.5194/acp-17-1329-2017](https://doi.org/10.5194/acp-17-1329-2017), 2017.~~

1237 ~~Yue, X., Unger, N., Harper, K., Xia, X., Liao, H., Zhu, T., Xiao, J., Feng, Z., and Li, J.:~~  
 1238 ~~Ozone and haze pollution weakens net primary productivity in China, *Atmospheric*~~  
 1239 ~~*Chemistry and Physics*, 17, 6073-6089, [10.5194/acp-17-6073-2017](https://doi.org/10.5194/acp-17-6073-2017), 2017.~~

1240 ~~Yue, X., and Unger, N.: Fire air pollution reduces global terrestrial productivity, *Nature*~~  
 1241 ~~*Communications*, 9, 5413, [10.1038/s41467-018-07921-4](https://doi.org/10.1038/s41467-018-07921-4), 2018.~~

1242 Yue, X., Zhang, T., and Shao, C.: Afforestation increases ecosystem productivity and  
 1243 carbon storage in China during the 2000s, ~~*Aggr*~~*Agricultural and Forest*  
 1244 ~~*Meteorol*~~*Meteorology*, 296, 108227, [10.1016/j.agrformet.2020.108227](https://doi.org/10.1016/j.agrformet.2020.108227), 2021.

1245 ~~Zhang, Y., Li, C., Trettin, C. C., Li, H., and Sun, G.: An integrated model of soil,~~  
 1246 ~~hydrology, and vegetation for carbon dynamics in wetland ecosystems, *Global*~~  
 1247 ~~*Biogeochemical Cycles*, 16, 9-1-9-17, <https://doi.org/10.1029/2001GB001838>,~~  
 1248 ~~2002.~~

1249 ~~Zhang, Z., Zimmermann, N. E., Stenke, A., Li, X., Hodson, E. L., Zhu, G. F., Huang,~~  
 1250 ~~C. L., and Poulter, B.: Emerging role of wetland methane emissions in driving 21st~~  
 1251 ~~century climate change, *P Natl Acad Sci USA*, 114, 9647-9652,~~  
 1252 ~~[10.1073/pnas.1618765114](https://doi.org/10.1073/pnas.1618765114), 2017.~~

1253 Zhang, Z., Fluet-Chouinard, E., Jensen, K., McDonald, K., Hugelius, G., Gumbrecht,

Formatted: Indent: Left: 0 cm, Hanging: 1.77 ch, First line: -1.77 ch

Formatted: Indent: Left: 0 cm, Hanging: 1.77 ch, First line: -1.77 ch

Formatted: Indent: Left: 0 cm, Hanging: 1.77 ch, First line: -1.77 ch

Formatted: Indent: Left: 0 cm, Hanging: 1.77 ch, First line: -1.77 ch

Formatted: Indent: Left: 0 cm, Hanging: 1.77 ch, First line: -1.77 ch

1254 T., Carroll, M., Prigent, C., Bartsch, A., and Poulter, B.: Development of the global  
1255 dataset of Wetland Area and Dynamics for Methane Modeling (WAD2M), Earth  
1256 System Science Data, 13, 2001-2023, [10.5194/essd-13-2001-2021](https://doi.org/10.5194/essd-13-2001-2021), 2021.

~~1257 Zhang, Z., Zimmermann, N. E., Stenke, A., Li, X., Hodson, E. L., Zhu, G. F., Huang,~~  
~~1258 ~~C. L., and Poulter, B.: Emerging role of wetland methane emissions in driving 21st~~~~  
~~1259 ~~century climate change, P Natl Acad Sci USA, 114, 9647-9652, 2017.~~~~

1260 Zhu, Q., Liu, J., Peng, C., Chen, H., Fang, X., Jiang, H., Yang, G., Zhu, D., Wang, W.,  
1261 and Zhou, X.: Modelling methane emissions from natural wetlands by  
1262 development and application of the TRIPLEX-GHG model, Geosci Model Dev, 7,  
1263 981-999, [10.5194/gmd-7-981-2014](https://doi.org/10.5194/gmd-7-981-2014), 2014.

1264 Zhuang, Q., Melillo, J. M., Kicklighter, D. W., Prinn, R. G., McGuire, A. D., Steudler,  
1265 P. A., Felzer, B. S., and Hu, S.: Methane fluxes between terrestrial ecosystems and  
1266 the atmosphere at northern high latitudes during the past century: A retrospective  
1267 analysis with a process-based biogeochemistry model, Global Biogeochem Cy, 18,  
1268 GB3010, [10.1029/2004GB002239](https://doi.org/10.1029/2004GB002239), 2004.

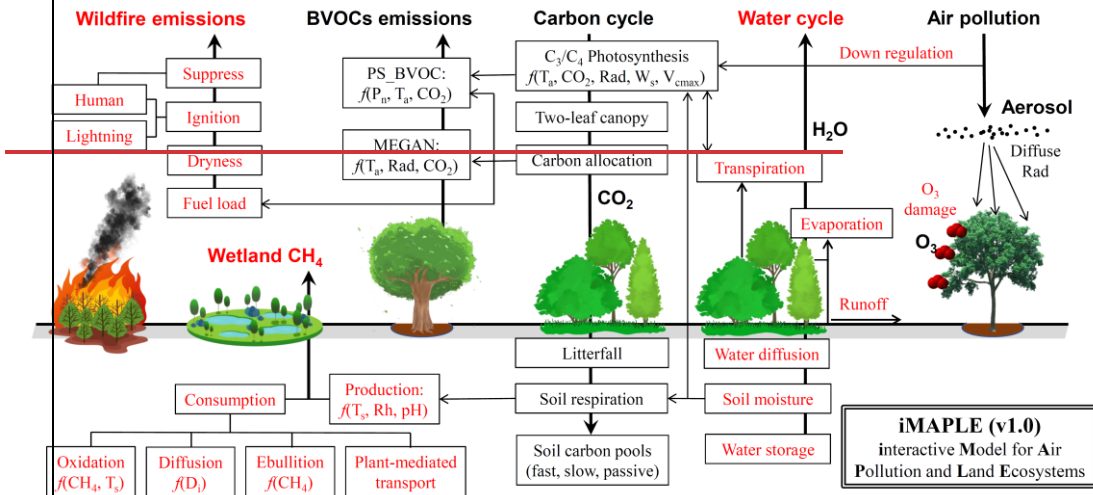
1269  
1270

Formatted: Indent: Left: 0 cm, Hanging: 1.77 ch, First line: -1.77 ch

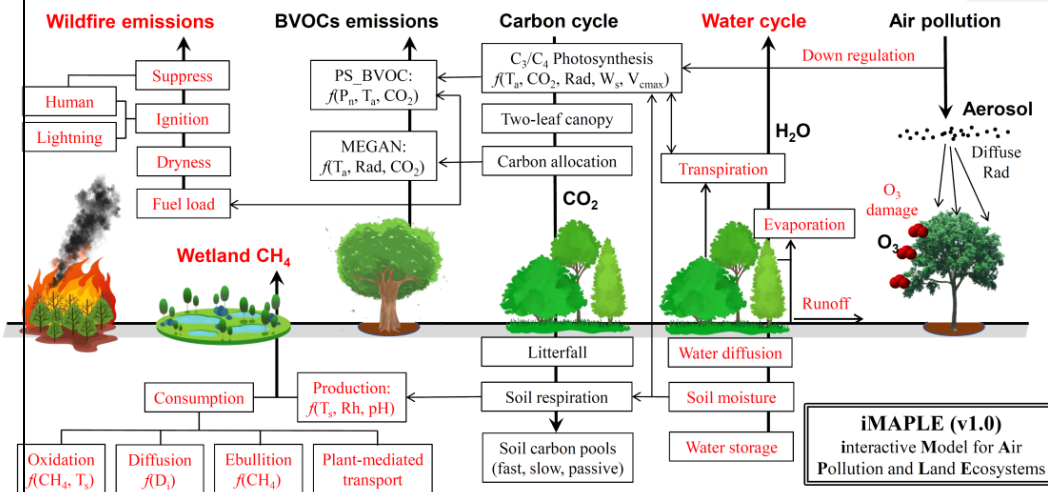
Formatted: Indent: Left: 0 cm, Hanging: 1.77 ch, First line: -1.77 ch, Line spacing: single



1271



1273

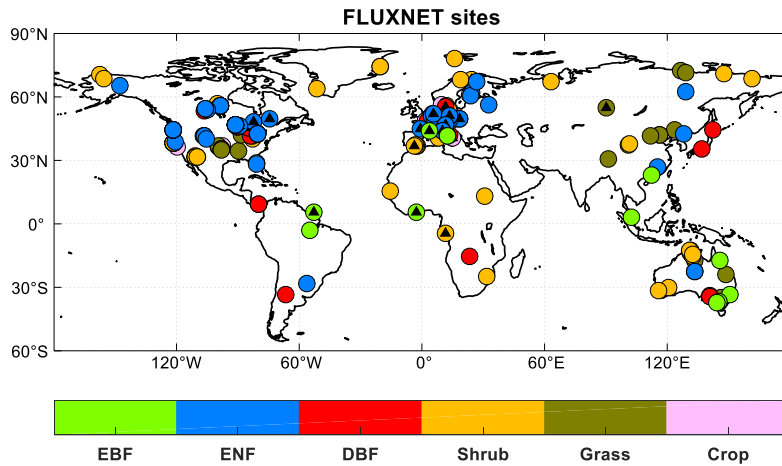


1275 **Figure 1** The illustration of biogeochemical processes in the iMAPLE version 1.0  
 1276 model. The carbon cycle is connected with water cycle, wildfire emissions, biogenic  
 1277 volatile organic compounds (BVOCs) emissions, wetland methane emissions, and is  
 1278 affected by air pollutants including aerosols and ozone. The bold arrows indicate the  
 1279 directions of fluxes and air pollutants. The thin arrows indicate the influential pathways  
 1280 among different components. The dependences on key parameters are shown for some  
 1281 processes. Red fonts indicate new or updated processes in iMAPLE relative to the YIBs  
 1282 model. For detailed parameterizations please refer to section 2.2.

1283

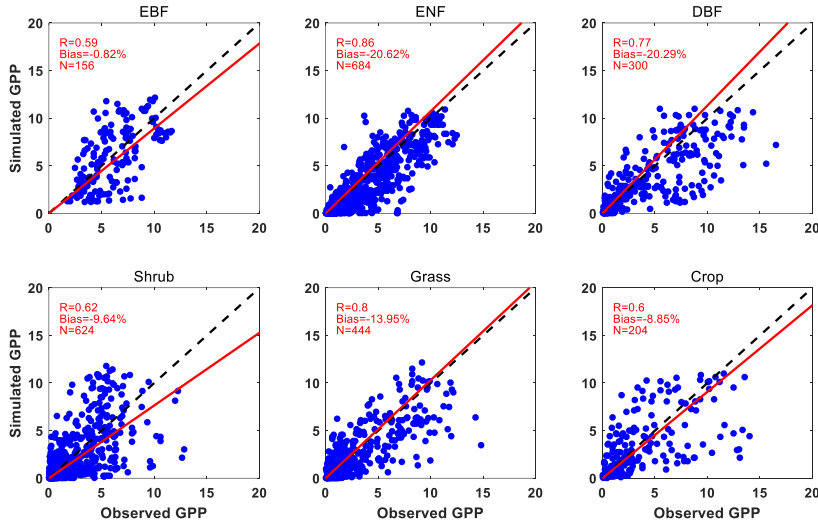
1284



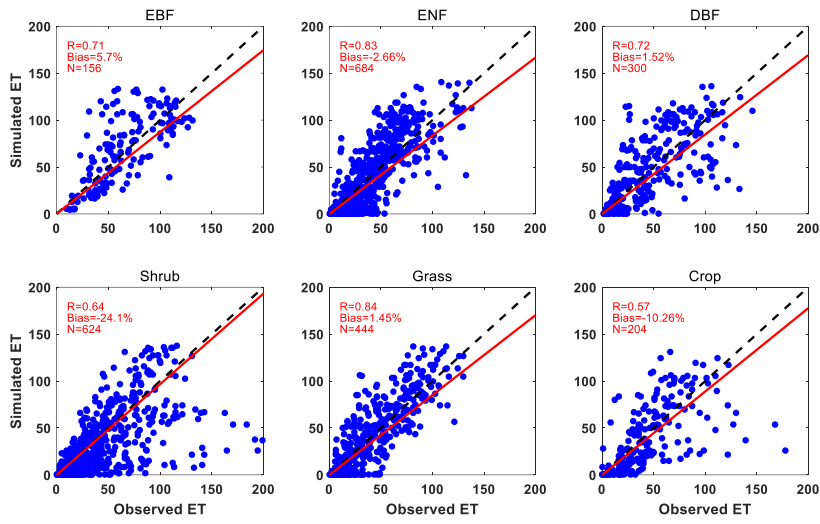


1285  
 1286  
 1287  
 1288  
 1289  
 1290  
 1291  
 1292

**Figure 2** Spatial distributions of 201 sites from global FLUXNET network. The colors indicate various plant functional types (PFTs) including evergreen broadleaf forest (EBF, 13 sites), evergreen needleleaf forest (ENF, 57 sites), deciduous broadleaf forest (DBF, 25 sites), Shrub (52 sites), Grass (37 sites), and Crop (17 sites). The black triangles indicate sites with at least one-year observations of diffuse radiation.

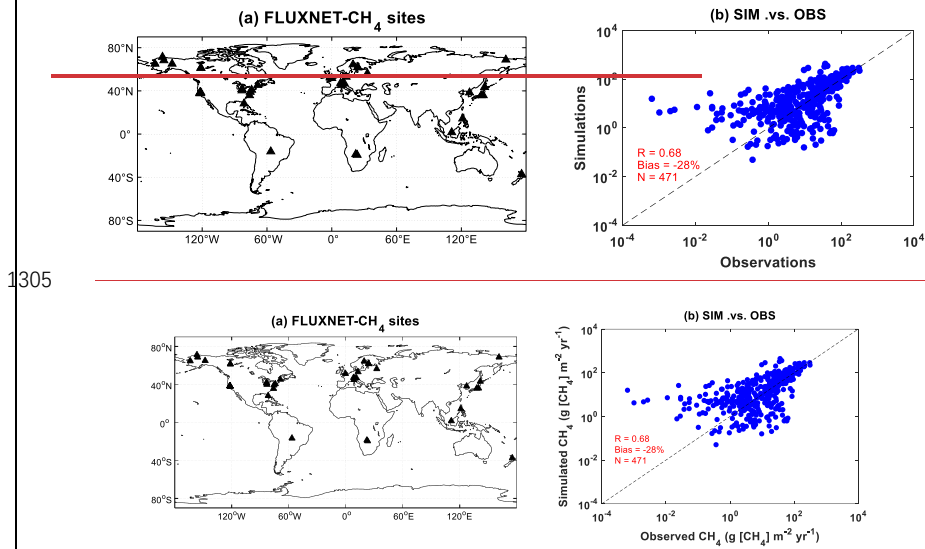


1293  
 1294 **Figure 3** Comparisons between observed and simulated monthly GPP from 201 FLUXNET sites.  
 1295 Each point indicates the average value of one month at a site. The red line represents linear  
 1296 regression between observations and simulations- from BASE experiment. The correlation  
 1297 coefficient (R), normalized mean bias and numbers of points/months (N) are shown on each panel.  
 1298 The comparisons are grouped into six PFTs including EBF, ENF, DBF, Shrub, Grass, and Crop. The  
 1299 unit is  $g\ C\ m^{-2}\ day^{-1}$ .  
 1300



1301  
 1302  
 1303  
 1304

**Figure 4** The same as Figure 3 but for ET. The unit is mm month<sup>-1</sup>.

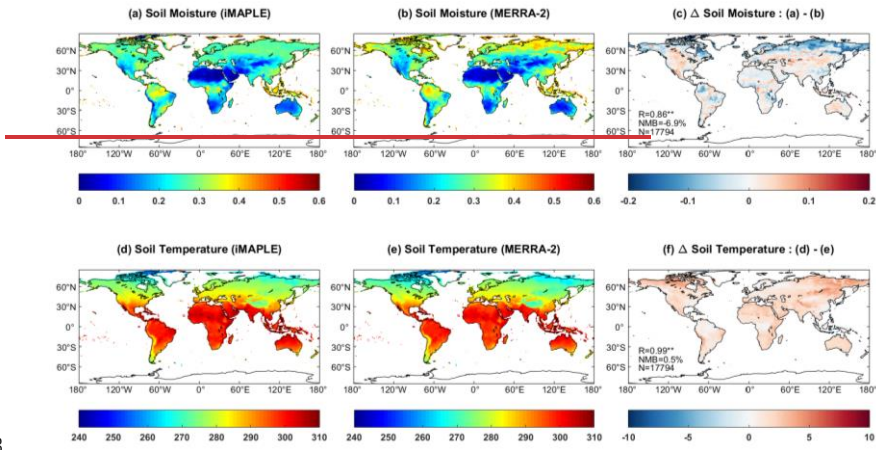


1305

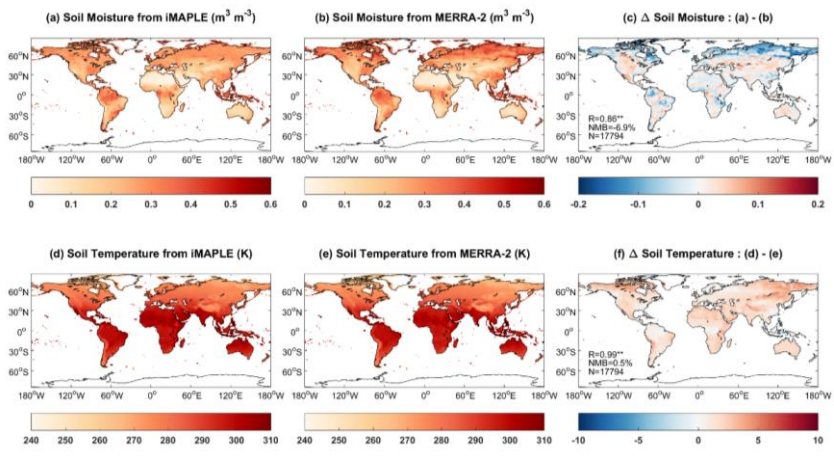
1306

1307 **Figure 5** (a) Spatial distribution of global FLUXNET-CH<sub>4</sub> sites and (b) comparisons between  
 1308 observed and simulated monthly methane flux from BASE experiment. Filled triangles indicate sites  
 1309 with at least six months observations of wetland CH<sub>4</sub> fluxes. Each point represents average value of  
 1310 monthly methane emission at one site. The correlation coefficient (R), normalized mean bias and  
 1311 numbers of points/months (N) are shown on the right panel. The unit is g [CH<sub>4</sub>] m<sup>-2</sup> yr<sup>-1</sup>.  
 1312

1313



1314

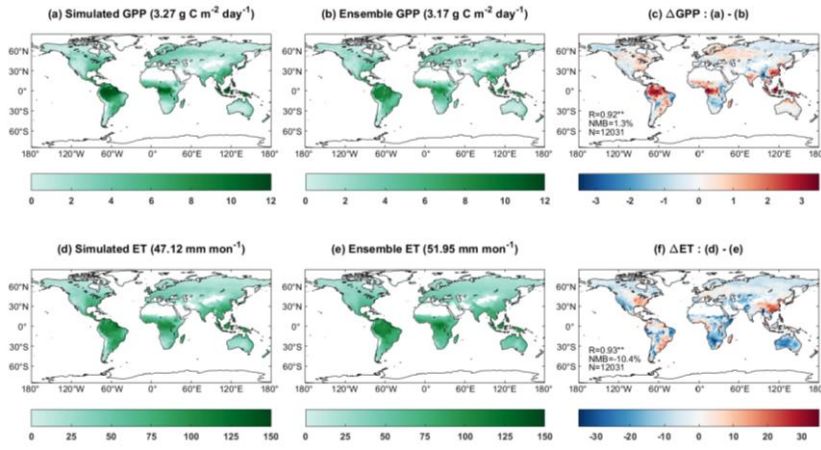


1315 **Figure 6** Comparisons of simulated (a) soil moisture ( $m^3 m^{-3}$ ) and (d) soil temperature (K) from the  
 1316 iMAPLE model with (b, e) the MERRA-2 reanalyses. Both simulations from BASE experiment and  
 1317 observations from MERRA-2 reanalyses are averaged for the period of 1980-2020. The spatial  
 1318 difference, correlation coefficient (R), normalized mean bias (NMB) between simulations and  
 1319 observations and numbers of points (N) are shown on (c) and (f), respectively.

1320

1321

1322



1323

1324

1325

1326

1327

1328

1329

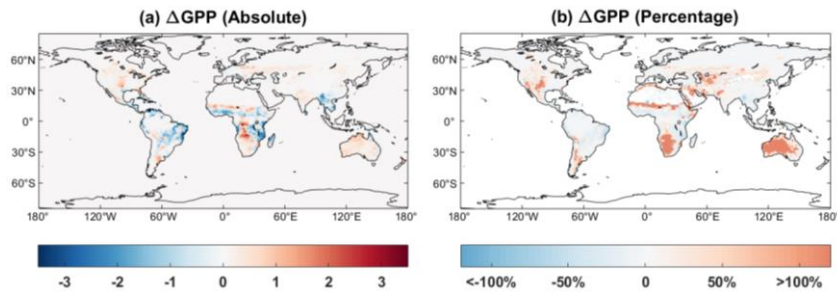
1330

1331

1332

1333

**Figure 7** Comparisons of simulated (a) gross primary productivity (GPP,  $\text{g C m}^{-2} \text{ day}^{-1}$ ) and (d) evapotranspiration (ET,  $\text{mm month}^{-1}$ ) with ensemble products from (b, e) observations. Simulated GPP and ET are performed by iMAPLE driven with meteorology from MERRA-2 reanalysis (BASE) during 2001-2013. Ensemble GPP products are from the average values of SIF-based GOSIF and satellite-based GLASS GPP products. Ensemble ET products include FLUXCOM and GLASS products during 2001-2013. The spatial difference, correlation coefficient (R), normalized mean bias (NMB) between simulations and observations and numbers of points (N) are shown on (c) and (f). Only land grids with vegetation are shown on each panel, and their area-weighted values are shown in titles.



1334

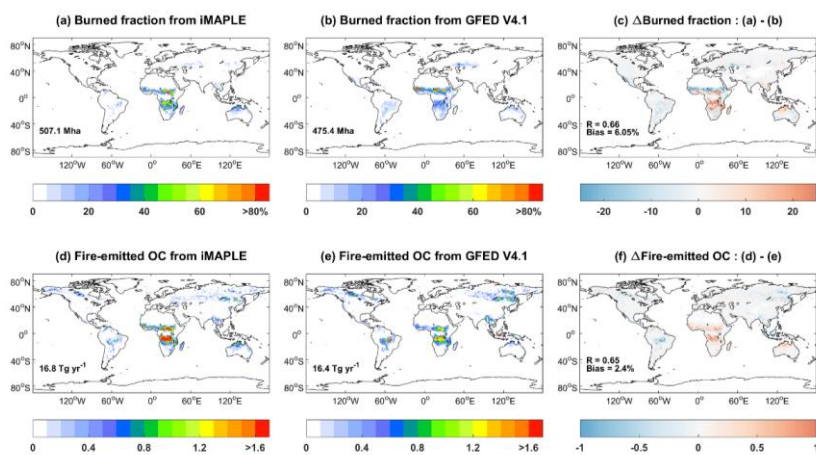
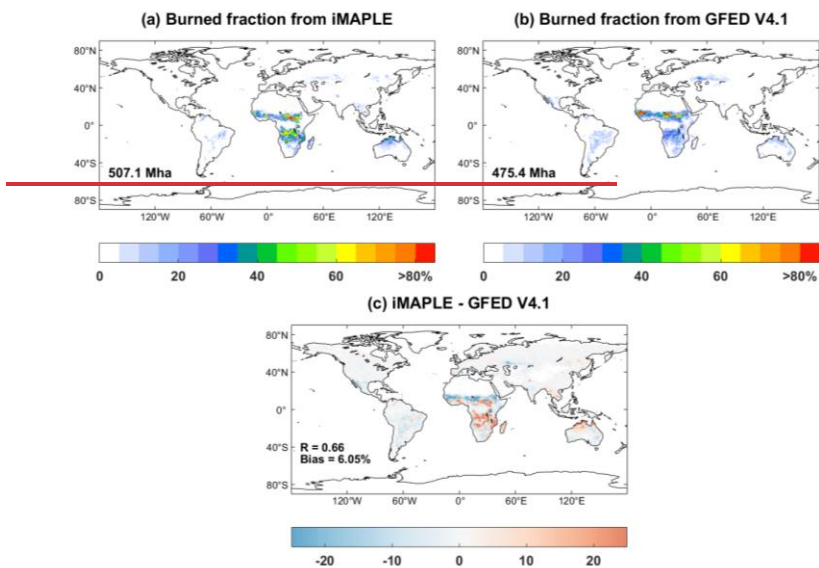
1335

1336

1337

1338

**Figure 8** Absolute ( $\text{g C m}^{-2} \text{ day}^{-1}$ ) and relative (%) differences of global GPP between simulations with (BASE) and without (BASE NW) two-way carbon-water coupling processes. Simulation results are averaged for the period of 1980-2020.



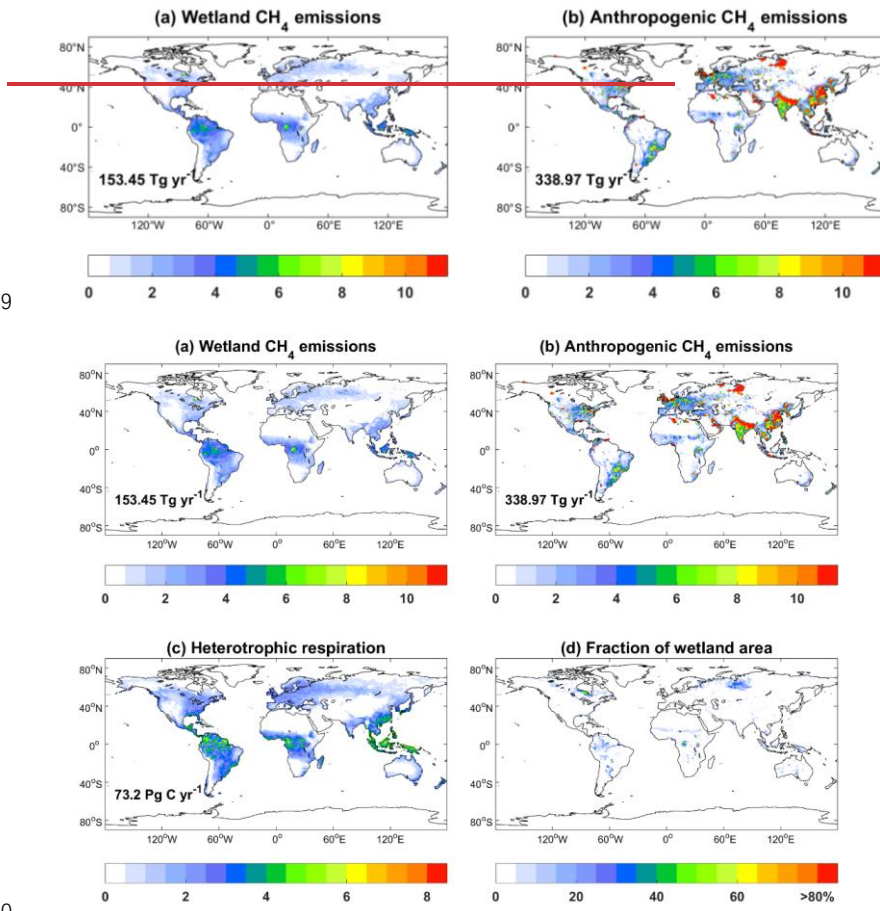
1339

1340

1341 **Figure 9** Comparisons of global burned fraction (%) and fire-emitted OC emissions ( $10^{-3} \text{ kg km}^{-1}$   
 1342  $\text{yr}^{-1}$ ) between (a, d) simulations and (b, e) observations. Simulations are performed using iMAPLE  
 1343 and observations are from GFED V4.1 fire emissions products. Both simulations from BASE  
 1344 experiment and observations are averaged for the 1997-2016 period. The global total area burned  
 1345 are shown on (a) and (b), and total OC emissions are shown on (d) and (e). The spatial difference,  
 1346 correlation coefficient (R), and normalized mean biases between simulations and observations  
 1347 are shown on (c) and (f).  
 1348



1349



1350

1351

1352

1353

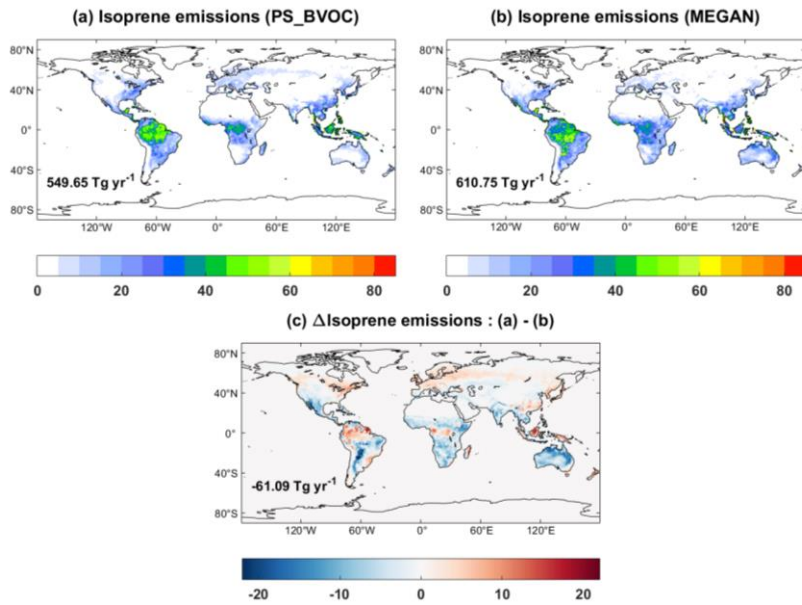
1354

1355

1356

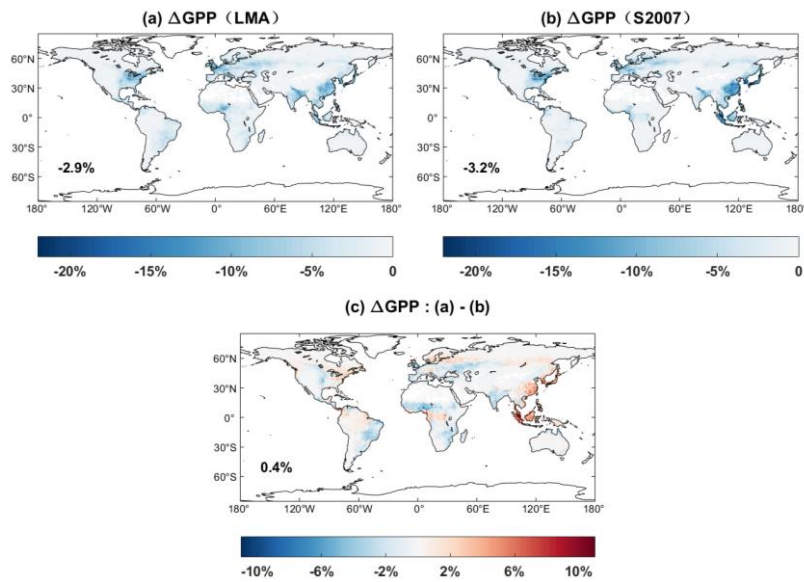
1357

**Figure 10** Global simulated CH<sub>4</sub> emissions (g [CH<sub>4</sub>] m<sup>-2</sup> yr<sup>-1</sup>) from (a) wetland and (b) anthropogenic sources, (c) heterotrophic respiration (gC m<sup>-2</sup> day<sup>-1</sup>) and (d) fraction of wetland area. The simulations are from BASE experiment. Anthropogenic sources include are adopted from CMIP6 including the sectors of energy, agriculture, industrial, residential, shipping, solvent and transportation. The global total emissions and heterotrophic respirations are shown on each panel. Both the wetland and other emissions All variables are averaged for 2000-2014.



1358  
 1359  
 1360  
 1361  
 1362

**Figure 11** Global isoprene emissions ( $\text{mg C m}^{-2} \text{ day}^{-1}$ ) from (a) MEGAN, (b) PS\_BVOC schemes and (c) their differences during 1980-2020. The simulations are from BASE experiment. The global total emissions are shown on each panel.



1363

1364

1365

1366

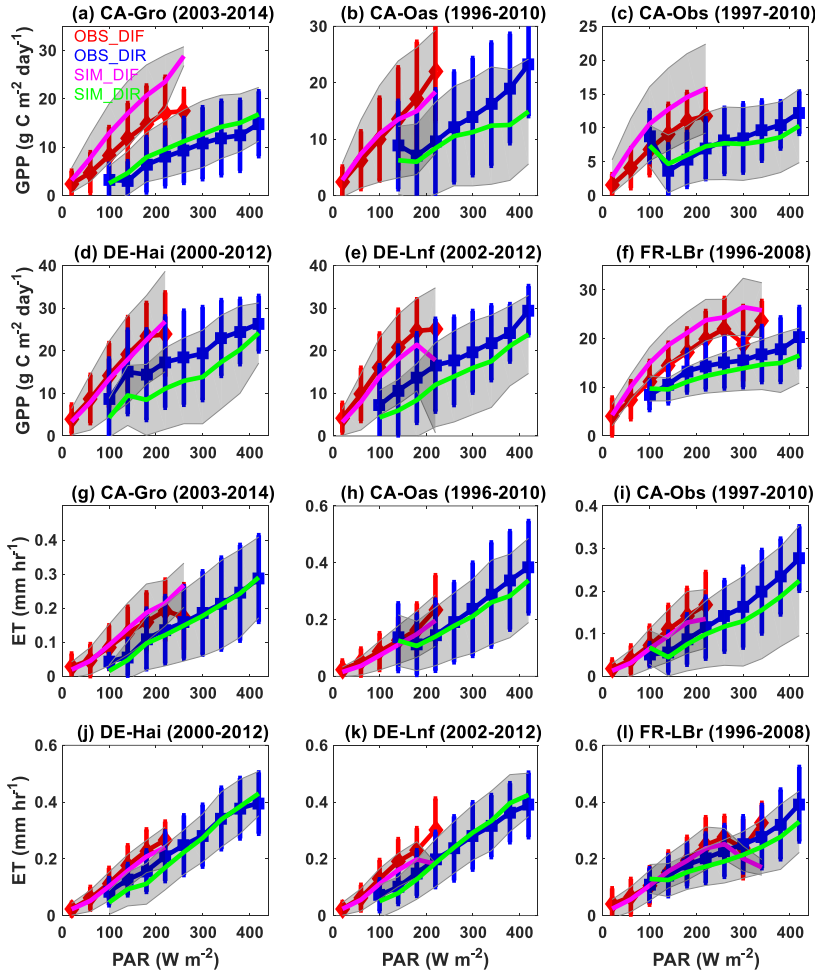
1367

1368

1369

1370

**Figure 12** Percentage changes of global GPP caused by ozone damage effects: based on (a) LMA (O3LMA-BASE) and (b) S2007 (O3S2007-BASE) schemes. The ozone damage schemes include (a) trait leaf mass per area (LMA)-based from O3LMA experiment, (b) S2007 plant ozone sensitivity from O3S2007 experiment and (c) their differences.



1371

1372

1373

1374

1375

1376

1377

1378

1379

1380

**Figure 13** Observed and simulated responses of site-level (a-f) GPP and (g-l) ET to diffuse and direct radiation at the FLUXNET sites. Photosynthetically active radiation (PAR) reaching the surface are divided into diffuse (diffuse fraction > 0.75) and direct (diffuse fraction < 0.25) radiation at six FLUXNET sites with more than 10 years of observations. Observations (simulations) are grouped over PAR bins of 40 W m<sup>-2</sup> with errorbars (shadings) indicating standard deviations of GPP and ET for each bin. The red (blue) and magenta (green) represent observed and simulated responses of GPP and ET to diffuse (direct) radiation. Units of GPP and ET are g C m<sup>-2</sup> day<sup>-1</sup> and mm hr<sup>-1</sup>, respectively.